Geophysical Investigation of the Yellowstone Hydrothermal System

Kira A. Dickey

Thesis submitted to the Faculty of the
Virginia Polytechnic Institute and State University
in partial fulfillment of the requirements for the degree of

Master of Science
in
Geophysics

W. Steven Holbrook, Chair
Scott King
Carol A. Finn

July 5, 2018
Blacksburg, Virginia

Keywords: Geophysics, Airborne EM, Aeromagnetics, Yellowstone

Geophysical Investigation of the Yellowstone Hydrothermal System

Kira A. Dickey

ABSTRACT

Yellowstone National Park hosts over 10,000 thermal features (e.g. geysers, fumaroles, mud pots, and hot springs), yet little is known about the hydrothermally active zones hundreds of meters beneath the features. Transient electromagnetic (TEM) soundings and 2D direct current (DC) resistivity profiles show that hydrothermal alteration at active sites have a higher electrical conductivity than the surrounding hydrothermally inactive areas. For that reason, airborne TEM is an effective method to characterize large areas and identify hydrothermally active and inactive zones using electrical conductivity. Here we present results from an airborne TEM survey acquired jointly by the U.S. Geological Survey and the University of Wyoming in November, 2016. We integrate resistivity from the airborne electromagnetic (EM) survey with research drillhole data and rock physics models to investigate the controls on electrical conductivity in the upper few hundreds of meters of the Yellowstone hydrothermal system. Resistivities in Yellowstone are the product of complex variations of lithology, temperature, salinity, clay content, and hydrothermal fluids. Results show that the main drivers in lowering the high resistivitiy of volcanic rocks are water saturation and hydrothermal alteration. Salinities are not significantly elevated in Yellowstone and temperature is not a first order affect.

Geophysical Investigation of the Yellowstone Hydrothermal System

Kira A. Dickey

GENERAL ABSTRACT

Yellowstone National Park is a popular scientific and tourist destination because of it's vast amount of thermal features including hot springs like Grand Prismatic, geysers like Old Faithful, and many more. But what is happening beneath those features and how can we use geophysics to find out? In November 2016, the U.S. Geological Survey and University of Wyoming conducted an airborne geophysical survey that measures how conductive the rock is beneath Yellowstone. Using this data, we map fluids and hydrothermal activity, and relate them to the local geology. The goal of this thesis is to understand the geologic factors that make the rock beneath Yellowstone's features conductive. We have shown that the main factors that contribute to the high conductivities in thermal areas of Yellowstone are hydrothermal alteration of the rocks and the high amount of fluids filling space inside the rocks.

Contents

List of Figures

Introduction

Yellowstone National Park is home to the world's most extensive terrestrial hydrothermal system, containing the most abundant hot springs in the world, a variety of unique biological life forms, and over 10,000 thermal features (Hurwitz & Lowenstern, 2014). These unique features are driven by active volcanism, which, unlike most of the Earth's volcanic and tectonic features, is found ∼2,000 km from the nearest plate boundary, and it is known as the Yellowstone "hot spot" (Smith & Braile, 1994). The migration of the North American Plate over the Yellowstone hot spot produced the northeast-trending Yellowstone-Snake River Plain volcanic system, which is currently active in Yellowstone National Park (Smith & Braile, 1994). Within the park is the Yellowstone Plateau Volcanic Field, which formed over the last 2 million years in three main cycles of volcanism (R. L. Christiansen, 2001). The Yellowstone Plateau spans an area of over 6,500 km^2 and is comprised of an accumulation of rhyolite and basalt (Smith & Christiansen, 1980). Aside from volcanic activity, Yellowstone is also the most seismically active zone within the Intermountain Seismic Belt (Waite & Smith, 2002). The combination of volcanic and tectonic processes provide fracture systems through which hot fluids circulate and rise to the surface, driving Yellowstone's variety of prominent hydrothermal features (Pitt & Hutchinson, 1982).

Although the park is a major tourist destination and has been extensively studied, little is known about the hydrothermal structure hundreds of meters beneath Yellowstone's promi-

nent features. Smaller scale 2D direct current (DC) resistivity and electromagnetic (EM) surveys in the park show increased electrical conductivity in active thermal areas (Pasquet et al., 2016; Zohdy et al., 1973; Munoz, 2014); however, these surveys are difficult to conduct over the large areas needed to investigate the plumbing of the entire hydrothermal system. For this reason, the University of Wyoming and U.S. Geological Survey, in coordination with the Hydrogeophysics Group of Aarhus University, flew an airborne transient electromagnetic (TEM) survey over large areas of Yellowstone National Park in November, 2016. The survey covers extensive areas over active hydrothermal zones and has a depth of investigation ranging between 200 and 300 meters over active hydrothermal areas. The motivations behind this survey include implications for hazard assessment within the park, identification of the extents of alteration beneath active zones, and geothermal resource applications outside the park. Since Yellowstone is protected from geothermal energy and mineral exploration, the park provides unique opportunities to study an undisturbed hydrothermal system (Hurwitz & Lowenstern, 2014).

This paper investigates segments of the airborne TEM survey near 11 research drillholes (White et al., 1975; Fenner, 1936) in order to link lithology, temperature, and fluid conductivity to the electrical resistivity structure of Yellowstone National Park. Geothermal areas have many physical factors that increase electrical conductivity; therefore the interpretation of hydrothermally altered zones is complex. We integrate research drilling data and rock physics to investigate the rock properties that decrease resistivities in active areas throughout Yellowstone. We study lithologic controls on resistivity and use rock physics models to understand the effects of temperature, percent water, and clay content on resistivity. The two main focus areas of this paper are the Norris Basin and the Geyser Basins (Upper, Midway, and Lower), which have airborne TEM coverage and borehole data in thermal areas. The results show that temperature and porosity do not show a first-order correlation

with resistivities; rather, they enhance hydrothermal alteration and clay deposition which greatly decrease resistivity. Water saturation levels drastically reduce electrical resistivities. In Yellowstone, given the large amount of meteoric water and shallow water table, we can assume that rocks with porosities above ∼10% have water in the pore spaces. Lithology has a variable effect on resistivities depending on the degree of alteration. These conclusions will aid in the interpretation of the airborne EM data over the park.

1.1 Regional Geology

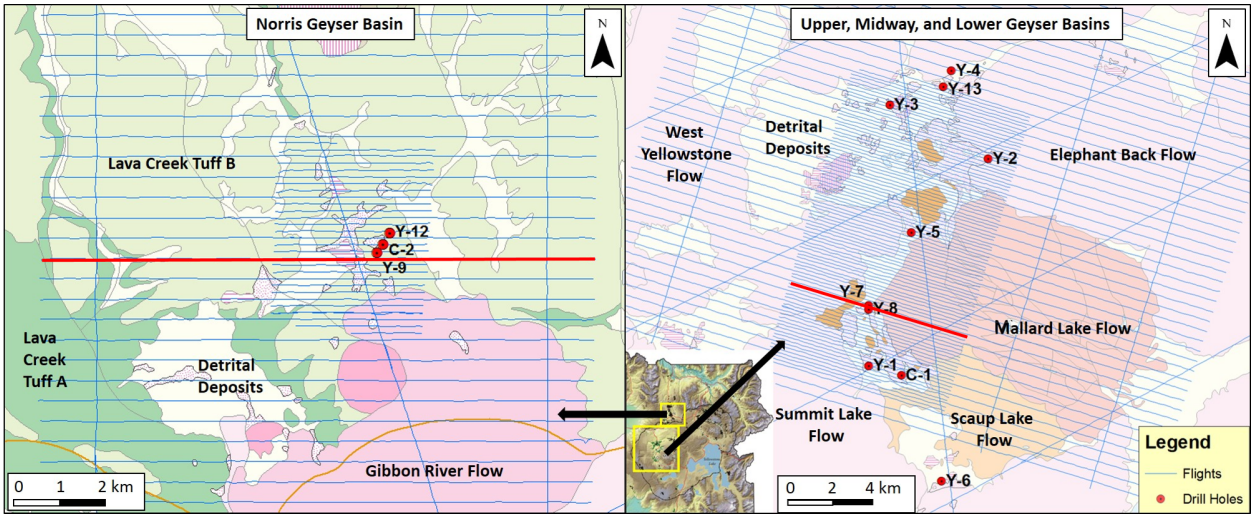

Figure 1.1: Geologic maps of the Geyser Basins (right) and Norris Basin (left) including drillholes and flight lines. Outlined red flight lines are lines 11660 (Norris) and 33680 (Geyser Basins) used in Figures 3.1 and 3.2. Geology: pinks = Rhyolite 160ka - 70ka, orange = Rhyolite 160ka - 640ka, green = Lava Creek Tuff ∼640ka (R. L. Christiansen, 2001)

In the past 2.1 million years, there have been three major ash-flow eruptions of the Yellowstone Volcano (R. L. Christiansen, 2001). The first and largest eruption occurred 2.1 million years ago and deposited the Huckleberry Ridge Tuff, creating a caldera over 75 km wide (R. L. Christiansen, 2001). Next, the Mesa Falls Tuff was deposited during the second and smallest eruption 1.3 million years ago (R. L. Christiansen, 2001). The current Yellowstone

Caldera was formed 640,000 years ago during the most recent of the last three major eruptions, which distributed the Lava Creek Tuff (R. L. Christiansen, 2001). The caldera has since been infilled with at least 30 smaller rhyolite flows occupying over 900 km^3 in volume (Waite & Smith, 2002; R. L. Christiansen, 1984). In hydrothermal areas, the rhyolite flows are generally overlain with sediments and and sinter (White et al., 1975).

The stratigraphy of drillholes within the Geyser Basin hydrothermal areas is predominantly accumulations of rhyolite flows that infill the caldera, all overlain with glacial sediments and a thin layer of sinter, denoted by "detrital deposits" (Figure 1.1) (White et al., 1975). The stratigraphy within Norris Basin drillholes shows thinner layers of glacial sediments and sinter overlaying massive Lava Creek Tuff Members A and B. The Lava Creek Tuff is the oldest rhyolite flow within the caldera as it was deposited during the last major eruption (640ka) (R. L. Christiansen & Blank Jr, 1972). Only the Y-5 hole in the Geyser Basins penetrates the Lava Creek Tuff, which is overlain glacial sediments (White et al., 1975).

The Lava Creek member A is exposed mainly in western and north-central Yellowstone, and is thickest (490 m) around Purple Mountain in northwest Yellowstone (R. L. Christiansen, 2001). Member A is 100-400 meters thick within the Geyser Basins, and thins between Norris Basin and Mammoth Hot Springs (R. L. Christiansen, 2001). On the contrary, the Lava Creek Tuff member B is widely exposed throughout the park, and thickens over the Norris Mammoth Corridor (R. L. Christiansen, 2001). The younger flows (e.g. the West Yellowstone Flow, Nez Perce Flow, Elephant Back Flow) that infill the caldera make up the Central Plateau Member. These flows vary in thickness and volume; the thickest deposited is nearly 300 meters thick and 32 km wide (R. L. Christiansen, 2001).

Methods

Yellowstone has been a research destination for a variety of disciplines including biology, geology, geochemistry, and geophysics. Many smaller scale geophysical surveys have been effective in characterizing localized geothermal activity; however, most do not have the ability to penetrate to depths of hundreds of meters, nor collect data over expansive areas. These surveys include 2D and 3D resistivity, refraction and reflection seismology, ground-based EM, and borehole drilling. Aeromagnetic data was collected over the entire park in 1999 and was effective in mapping geologic units; however, unlike electrical conductivity methods, magnetics cannot map water or thin layers of alteration. We incorporate the results from research drilling into our analysis of Yellowstone's physical properties.

2.0.1 Airborne EM and Aeromagnetics

The University of Wyoming and the U.S. Geological Survey (USGS), in coordination with the HydroGeophysics Group Aarhus University, Denmark (HGG), jointly acquired over 4100 km of airborne TEM and magnetic data over Yellowstone National Park in November 2016. The EM survey was flown using the SkyTEM 312. The airborne TEM method was chosen due to the large amount of electrical conductivity data that can be acquired in minimal time, making it ideal for geophysical mapping of a large hydrothermal system. Areas of

focus for this survey were Geyser Basins (Upper, Midway and Lower), Norris-Mammoth Corridor, Mud Volcano Area, caldera boundaries, and Yellowstone Lake; this paper focuses on resistivity data from the Geyser Basins and Norris Basin. Airborne data were acquired with 450 meter line spacing with 150 meter infills for more detailed mapping over Norris Basin and the Geyser Basins (see Figure 1.1). The average flight speed was 21 m/s, and the average flight altitude was 38 meters (frame height), with variations depending on terrain roughness. Survey lines were oriented perpendicular to fault strike directions and general trends of hydrothermal areas.

2.0.2 Instrumentation

The SkyTEM 312 is a dual-moment instrument that works by flying a transmitter loop and receiver loop over the target area with a helicopter. Current is turned on in the transmitting loop, creating an electric field that induces secondary eddy currents in the conductive subsurface, which in turn produce a secondary electromagnetic field that is recorded by the receiver loop when the current is turned off. The dual-moment transmitter provides high- and low-moment data that provides high resolution in the shallow subsurface as well as the ability to penetrate deeper layers up to 600 meters. A depth of investigation (DOI) is estimated for each resistivity model, as described in A. Christiansen & Auken (2012). For this survey, most DOI's in thermal areas were ∼200 meters and ∼400 meters in resistive areas. The SkyTEM system transfer function, the number of data points, the data uncertainty, and the resistivity model are each considered in order to calculate the DOI. Inversion results below the DOI are not considered reliable and are therefore not shown. The depth of investigation is between 200 meters and 300 meters for resistivity lines shown in this thesis. More information about the SkyTEM 312 can be found in Sørensen & Auken (2004), and further explanations of the TEM method can be found in Nabighian & Macnae (1991) and

Jørgensen et al. (2003).

Aeromagnetic data was also acquired during the airborne survey using the Geometrics G822A sensor and Kroum KMAG4 counter, which is a high-sensitivity Cesium magnetometer. The magnetometer is synchronized with the TEM such that measurements were taken when the TEM signal was off. The data were averaged and sampled at 50 Hz.

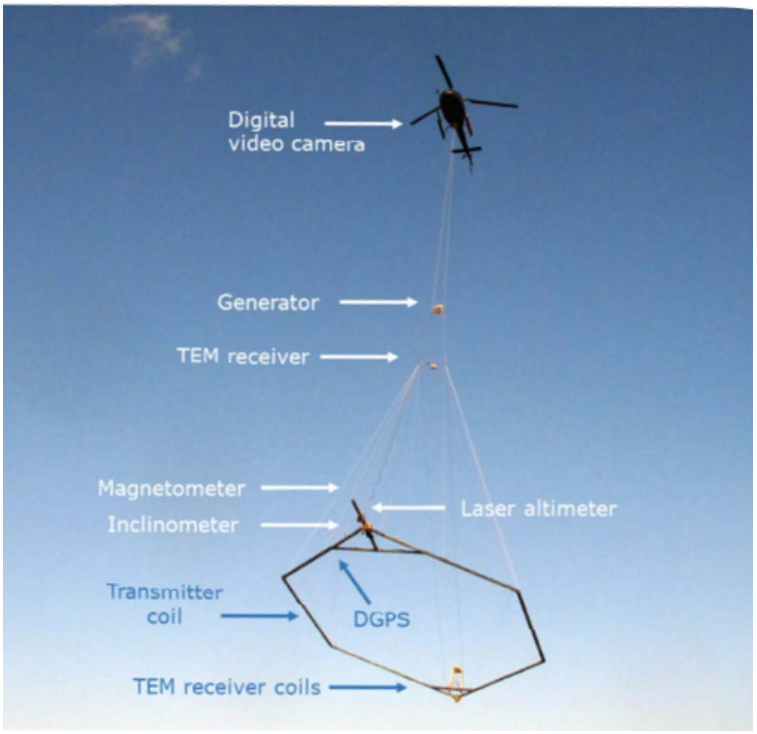

Figure 2.1: SkyTEM set up from *SkyTEM, Appendix A, Specifications of the SkyTEM312 System 60 Hz*

2.0.3 EM Inversion

Two types of inversion schemes were applied to the airborne EM data. A 2-D LCI (laterally constrained inversion) scheme was used for the inversion of each line. A 3-D SCI (spatially constrained inversion) scheme was used to invert the EM data to 3-D block models within Norris Basin and the Geyser Basins.

The 2D profiles shown in this thesis were calculated using a LCI scheme, which uses single line data as lateral constraints but does not incorporate data from adjacent lines. Inversions were performed using the Aarhus Workbench software package, specifically the AarhusInv inversion code (Auken et al., 2014). The raw data collected during the survey are high and low-moment voltage data recorded approximately every 1.33 seconds. The average speed of the helicopter was 21 m/s; therefore raw data was collected every 25 to 30 meters. The raw EM data is processed to remove coupling and noise, then is stacked into soundings. The stacked raw soundings are inverted using a 1-D fully non-linear damped least-squares solution that outputs 1-D layered resistivity models. The 2-D profiles are generated by plotting all the 1-D resistivity inversions for each line by their UTM coordinates. Input parameters for the inversion include turn-on and -off ramps, front-gate, low-pass filters, and transmitter and receiver positions. Flight altitude from the laser altimeter is a model parameter and is manually corrected before inversion. We use a smooth inversion that penalizes rapid changes in resistivity with depth. Of the 817 km of line data processed in the Geyser Basins and Norris, only a few kilometers are shown in this paper. Further explanations of the EM data processing can be found in Appendix B.

A 3-D spatially constrained inversion (SCI) scheme was also performed. In the SCI, model is constrained between 1-D inversions along and across flight lines. This generates a 3-D model that can be viewed in horizontal slices and profiles. The 3-D model has spacing of about 50 by 52 meters laterally and 10 meter spacing with depth. These data were used to generate plots showing resistivities of hydrothermal and non-hydrothermal areas using multiple soundings.

2.1 Electrical Conductivity in Hydrothermal Areas

Electrical properties have been a powerful geophysical tool to map alteration and hydrothermal boundaries in hydrothermal and volcanic systems (Revil et al., 2002; Revil & Pezard, 1998; Finn et al., 2007; Ussher et al., 2000; Pasquet et al., 2016; Hatherton et al., 1966; Risk et al., 1999; Bibby et al., 1992). Geothermal systems can contain many factors that contribute to the reduction of resistivity, including increased temperature, high clay content, and saturation of rocks with conductive saline fluids. Although Yellowstone fluids generally have low salinity (Nordstrom et al., 2009), the other factors are present and variable in the Yellowstone hydrothermal system. Hot, conductive hydrothermal fluids decrease resistivity, as well as alter the host rock, producing clay mineral species that greatly decrease resistivity (Caldwell et al., 1986). Therefore, active hydrothermal zones have a combination of higher temperatures, clay content, and conductive fluids whereas inactive zones do not. Paleo thermal areas also exhibit clay minerals and alteration, but do not necessarily have high temperatures. For this reason, altered active and fossil hydrothermal areas have low resistivities, sometimes reaching single digits (Ussher et al., 2000; Revil et al., 2002). In contrast, fresh, unaltered volcanic rock has resistivities from high hundreds to 15,000 Ωm depending on the existence of fluids in the pore spaces (Finn et al., 2007, 2018).

The University of Wyoming conducted 2D and 3D resistivity surveys in Yellowstone along with ground-based TEM and EMI in 2015 and 2016. The results showed that variations in electrical resistivity provide first-order boundaries of hydrothermal zones and can differentiate between hydrothermally altered and fresh volcanic areas (Pasquet et al., 2016).

2.2 Borehole Data

Thirteen research holes (Y-1 through Y-13) were drilled in 1967-1968 by the USGS to understand the shallow lithology and hydrology in principal thermal areas of Yellowstone (White et al., 1975). Most of the holes penetrated between 60 and 100 meters in depth, with a maximum depth of 332 meters at the Y-12 hole in the Norris Basin. The data acquired from the research drilling includes subsurface pressure and temperature measurements as well as lithologic descriptions and occasionally porosity measurements. The drillhole sites were selected to be in or adjacent to main upflow zones across the Geyser Basins and Norris Basin, distributed to include major hot spring areas and other dominant geothermal activity (White et al., 1975). One conclusion drawn from White's study is that temperature gradients from ∼30-80 m are mostly linear. We also incorporate lithology and temperature data from the Carnegie boreholes, C-I and C-II, which were drilled in 1929 and 1930. The locations of the drillholes are shown in Figure 1.1.

We compare the temperature analysis, lithologic descriptions, and porosity measurements from the borehole data to the resistivity measurements from the airborne EM survey. The drillholes used in this thesis are Y-1, -2, -3, -5, -7, -8, -9, -12, -13, and C-I and C-II, which are the drillholes within the the extent of the airborne EM survey for the Geyser Basins and Norris Basin.

2.3 Rock Properties

In order to understand the resistivity values in Yellowstone, rock physics is used to relate resistivity, temperature, porosity, and clay content. The bulk electrical conductivity is dependent on porosity, the rock conductivity, fluid conductivity, and surface conductivity

(dependent on clay content). We start with a simple resistivity model that assumes no clay content, thus no surface conductivity, such that resistivity is only dependent on the resistivity of the saturating fluid, porosity, and subsurface temperature. We use Archie's (1941) empirical relationship for saturated rocks:

$$\rho = a\rho_w\phi^{-m} \tag{2.1}$$

where ρ is the rock resistivity, ϕ is the porosity, and ρ_w is fluid resistivity. The constants a and m are tortuosity and the cementation exponent and are empirically derived (Ussher et al., 2000). We assume that all rocks within the hydrothermal areas of Yellowstone are saturated due to the abundant fluids present while drilling the research holes and the shallow water table (generally ∼1 meter deep) (White et al., 1975). The formation factor, F, relates the rock resistivity and the fluid resistivity (Archie et al., 1942).

$$F = \frac{\rho}{\rho_w} \tag{2.2}$$

For sedimentary rocks, Archie's (1942) empirical relationship between the formation factor and porosity is:

$$F = a\phi^{-m} \tag{2.3}$$

Although this relationship was developed for sedimentary rocks, various studies have shown its effectiveness for volcanic rocks as well (Ahmed et al., 2018; Pezard, 1990; Jarrard & Schaar, 1991; Ildefonse & Pezard, 2001). These studies show that the resistivities of volcanic rock are

dominated by fluid conductivity of the pore space, as well as the surface conductance. For this study, we use $a = 2.4$ and $m = 2.12$, derived from measured rock samples in Yellowstone (Ahmed et al., 2018). We then use the Waxman-Smits equation, which incorporates clay content within the pore space. The Waxman-Smits equation for conductivity (reciprocal of resistivity) for a saturated shaley sandstone is:

$$\sigma_0 = \frac{1}{F^*}(\sigma_w + \sigma_e) \tag{2.4}$$

where F^* is the formation factor for the shaley sand, σ_0 is rock conductivity, σ_w is brine conductivity, and σ_e is clay conductivity (Waxman et al., 1968). The clay conductivity, which drives surface conductance, dominates the resistivity of altered rocks due the cation exchange capacity (CEC) of the clay (Revil et al., 2002, 2017; Revil, 2012; Ussher et al., 2000).

Other factors contributing to fluid resistivity include salinity and temperature. Drillhole measurements show increasing subsurface temperatures with depth, which may decrease resistivity. Hydrothermal fluids in Yellowstone have low salinity, indicating that salinity is likely not the main driver of low resistivities (Nordstrom et al., 2009). For the purposes of simple modeling, we use an NaCl concentration of 250 ppm to calculate fluid resistivity. Measured Cl^- concentrations range from 0.1 ppm to 669 ppm in thermal waters around the park, with higher concentrations in Norris (Fournier, 1989). Calculations using higher salinities were also done to test the minimum salinity needed to decrease resistivities to the values seen in near the drillholes. Previous studies including Revil et al. (2002, 2017) have measured resistivity related to temperature, salinity, and surface conductance of volcanic rocks. In order to implement temperature variations into the fluid resistivity calculation, we

use Dankov's (1962) relationship:

$$\rho_w = \frac{\rho_{w0}}{1 + \alpha(T - T_0)} \tag{2.5}$$

where ρ_{w0} is the fluid resistivity at temperature T_0, and α is the temperature coefficient of resistivity, which is dependent on salinity. Generally α=0.023°C^{-1} for a $T_0 = 23°C$; however we have calibrated α based on the Schlumberger model for resistivity of NaCl solutions (Schlumberger, 2009). Using the *Resistivity of NaCl Solutions Chart* and Arp's empirical relationship for resistivities of 250 ppm NaCl brine, we derive α and the corresponding T_0 and ρ_{w0}.

2.4 Magnetics

Electrical conductivity is a powerful tool when exploring hydrothermal systems due to the many factors that reduce resistivity in hydrothermally altered areas (Bibby et al., 1992). The alteration process also affects the magnetic properties of the host rock. In general, magnetite is one of the first minerals to be replaced during alteration (Browne, 1978). Magnetic studies of a variety of geothermal systems have associated magnetic lows with geothermal alteration (Finn & Morgan, 2002; Bouligand et al., 2014; Studt, 1959; Hochstein & Hunt, 1970; Björnsson et al., 1970). In particular, Finn & Morgan (2002) have associated negative magnetic anomalies in Yellowstone with hydrothermally altered areas, and positive anomalies with younger, fresh volcanic rocks. Therefore, we incorporate results from the aeromagnetic survey acquired in November 2016 with the electrical conductivity in two areas of the park.

Results

3.1 Magnetics

Resistivities at Norris Basin near Y-9 range from single digits to nearly 50 Ωm, and increase outwards into inactive areas to the east and west (Figure 3.1). The low resistivity zone is wider than the surficial geothermally altered area, but expands at depth to the west and east. The conductance plot shows increased conductance focused over the thermal areas and low conductance over the fresh volcanic rock. The average resistivity through the geothermal area is low compared to the fresh Lava Creek Tuff. To the west, the average resistivity has two broad highs which correlate with higher topography, suggesting lower porosity or fluid saturation at higher elevations. The magnetic profile also shows a magnetic low correlated with the geothermal area.

Figure 3.2 shows magnetics and electrical resistivity over the northern Upper Geyser Basin near drillholes Y-7 and Y-8. The Geyser basins vary more resistivities than Norris, and many laterally extensive conductive zones beneath inactive areas. Similar to Figure 3.1, the low resistivity zone reaches the surface in the same location as mapped geothermal alteration. This is also characterized by high conductance that gradually decreases over inactive areas. Average resistivities within the geothermal zone are single digits and rapidly increase to the west and east of the altered area. The average resistivity is more variable, with sharp

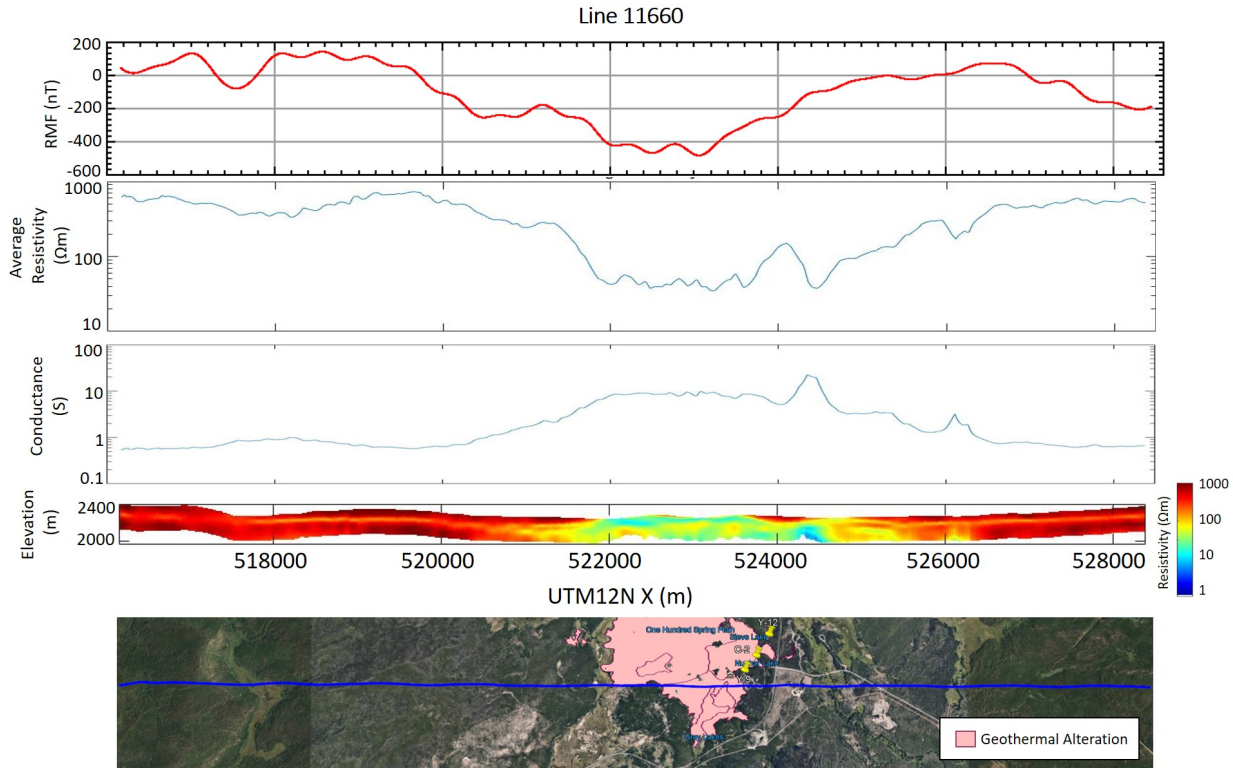

Figure 3.1: Line 11660 over the Norris Basin. The top panel shows the residual magnetic field (RMF) along the lines, which has been corrected to the International Geomagnetic Reference Field (IGRF), leveled, reduced to the pole, and filtered to eliminate surface noise. The second panel shows the average resistivity along the flight line, where the 1-D sounding is averaged over all depths above the DOI. The third panel shows the conductance which integrates conductivity and depth up to 300 meters. The fourth panel shows the 2-D resistivity profile along the flight line with a one to one scale. The bottom panel shows the aerial photo of the flight line and mapped geothermal areas from Google Earth.

decreases where subsurface resistivities begin to decrease near 50 meters depth. The residual magnetic field (RMF) shows a magnetic low over the altered area, but similarly to the average resistivity, has more variations. This is likely a result of surface geology, evident by the short wavelength of the anomalies. Because of the low altitude of the helicopter, the magnetometer measures small variations in surficial magnetization (e.g. surficial or shallow buried relatively unaltered rock).

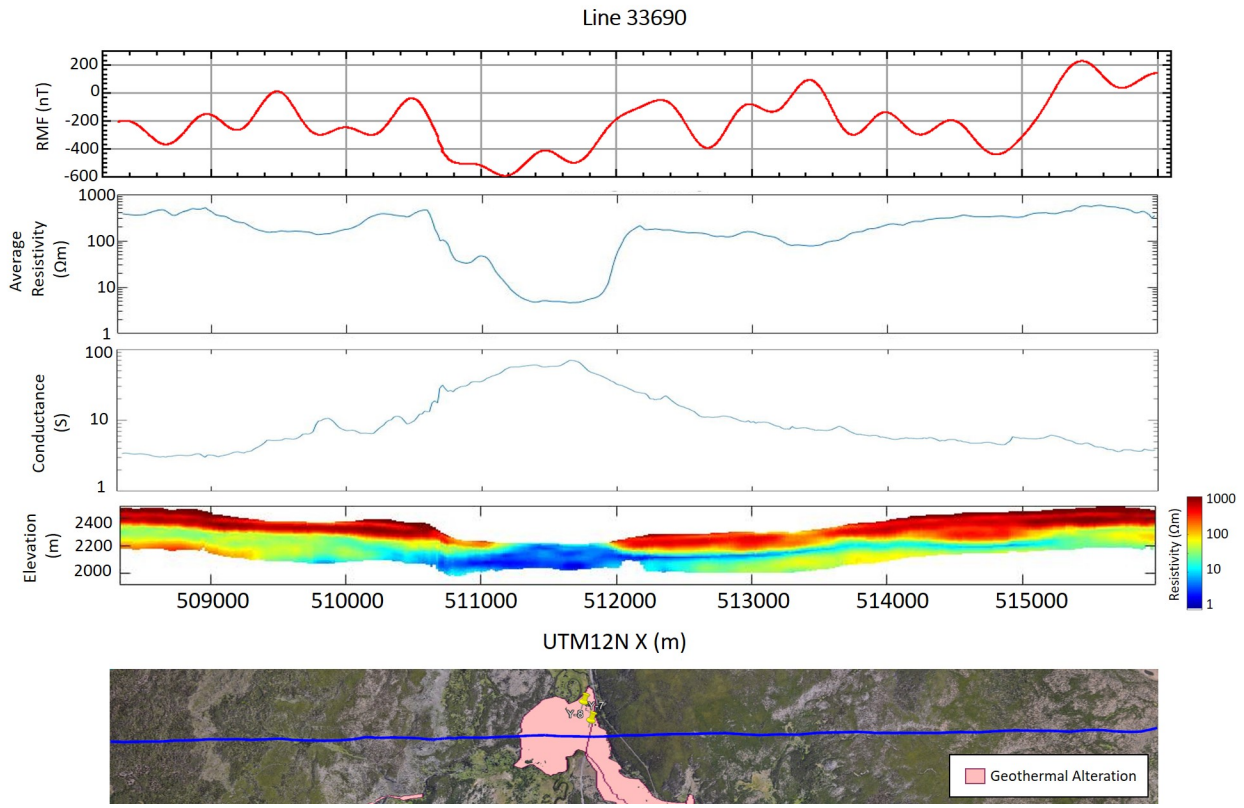

Figure 3.2: Line 33690 over the northern Upper Geyser Basin. The top panel shows the residual magnetic field (RMF) along the lines, which has been corrected to the International Geomagnetic Reference Field (IGRF), leveled, reduced to the pole, and filtered to eliminate surface noise. The second panel shows the average resistivity along the flight line, where the 1-D sounding is averaged over all depths above the DOI. The third panel shows the conductance which integrates conductivity and depth up to 300 meters. The fourth panel shows the 2-D resistivity profile along the flight line with a one to one scale. The bottom panel shows the aerial photo of the flight line and mapped geothermal areas from Google Earth.

3.2 Resistivity and Temperature

Temperature and resistivity have a poorly understood relationship, especially in hydrothermal systems. Temperature enhances alteration, making it common to find high degrees of alteration and clay, and therefore a higher CEC in hotter areas. This makes distinguishing temperature's effect on resistivity difficult because high CEC also lowers resistivity. To

further the complexity, fluid (electrolyte) resistivity and surface conductance are both dependent on temperature (Revil et al., 1998). Ussher et al. (2000) showed that increased temperature has a direct relationship with low resistivities for temperatures lower than 200°C, which make up the upper layer of the active geothermal system. However, for temperatures above 200°C, resistivities in hundreds of Ωm are measured (Ussher et al., 2000). Llera et al. (1990) showed a 6- to 11- fold increase in resistivity of volcanic rocks over a temperature increase from 30°C to 120°C using lab measurements. However, Flóvenz et al. (2005) and Hersir et al. (2013) showed that resistivities of basalt samples from geothermal fields in Iceland were dominated by high CEC from alteration rather than temperature. To test whether temperature is the main driver of decreased resistivities in Yellowstone, we compare the measured drillhole temperature with the resistivity data from the airborne EM survey at each drillhole location. It is worth noting that the temperatures used in this analysis are the more reliable temperature measurements from White et al. (1975), and only drillholes within the extent of the airborne survey over Norris and the Geyser Basins were used. The resistivities used to compare the borehole temperature are the nearest 1-D sounding to each drillhole from the 2-D resistivity profiles.

Figure 3.3 shows the measured down-hole temperatures for the drillholes and their corresponding resistivities. Also plotted is the calculated resistivity of Yellowstone volcanic rocks with 30% porosity (higher than average for Yellowstone rhyolites) with a salinity of 250 ppm, calculated using equations (1) and (5). This line represents an upper limit for resistivities at temperatures between 0°C and 250°C because it does not include clay content, which decreases resistivity. Overall, there is a slight negative correlation with high resistivities at lower temperatures and low resistivities at high temperatures; however, there is much variability; high temperatures (e.g. 180°C) have resistivities ranging from below 10 Ωm to nearly 100 Ωm. Low resistivities (e.g. 30 Ωm) have temperatures ranging from below 50°C

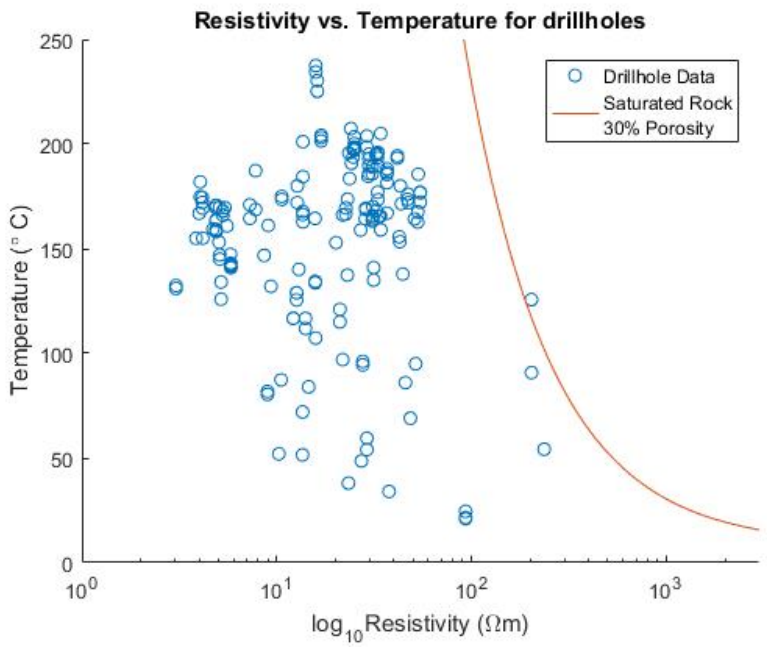

Figure 3.3: Temperature vs. resistivity plot of the research drillholes

to 200°C. In order to produce single- and double-digit resistivities seen in Yellowstone, clay content, therefore high CEC, must also be present. Ussher et al. (2000) similarly concluded that the low resistivities observed in geothermal systems are due to both high temperatures and the presence of conductive clays.

3.3 Porosity and Temperature Effects on Resistivity

Figure 3.4 shows predicted resistivity of saturated Yellowstone rocks with variable porosity and temperature calculated from Equations (1) and (5). Note that this model does not include clay content or surface conductance, which decrease resistivities by up to a factor of 12 depending on the type of clay present (Ussher et al., 2000). This model demonstrates the maximum resistivities expected to be seen in Yellowstone rocks given their porosity and temperature alone.

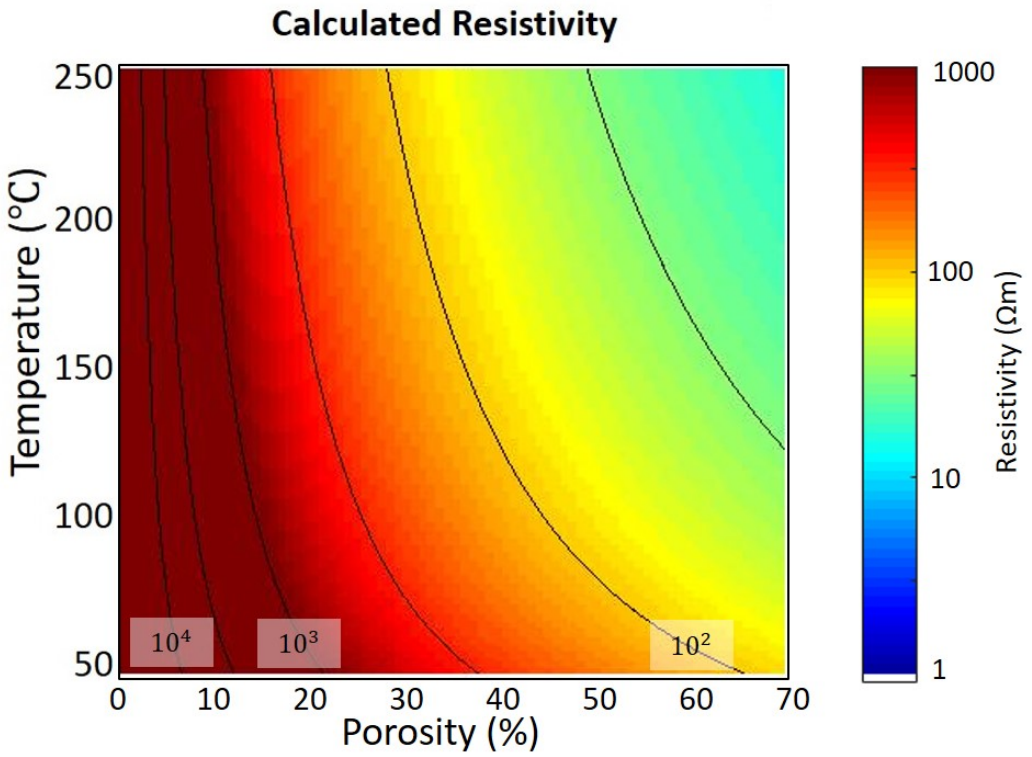

Figure 3.4: Maximum resistivity of Yellowstone rocks with variable porosity and temperature. Surface conductance is ignored.

Based on this model, at a constant temperature, resistivity can increase between two and three orders of magnitude from less than 10% porosity to 70% porosity, although 70% is not a practical value for lithologies in Yellowstone. In general, the glacial sediments in the uppermost lithologic layers have average porosities of 30% or higher (for Y-5, Y-7, and Y-8; 35% for Y-3) (Keith et al., 1978; Bargar & Beeson, 1985). The rhyolite and volcanic flows beneath the sediments have lower porosities, averaging between 15% and 20%, though pumiceous tuff reaches higher porosities, often over 40% (Keith et al., 1978; Dobson et al., 2003; Bargar & Beeson, 1985). Using a constant porosity of 20% for a rhyolite, a temperature increase from 50°C to 250°C causes the resistivity to drop from over 1000 Ωm to 300 Ωm. We assume that the temperature gradient is mostly linear (White et al., 1975). Even assuming the most porous possible pumiceous tuff (57% porosity, the maximum porosity of the Y-8

hole from Dobson et al. (2003)) at a temperature of 250°C, the resistivity reaches only 25 Ωm. In Yellowstone, resistivities reach single digits within rhyolite flows and sediments. Therefore, temperature alone cannot explain the lowest resistivities: there must also be a contribution of clays and alteration that drive resistivities to single digits. This is consistent with the magnetic lows in the altered areas; magnetics is not sensitive to temperature, fluid content or porosity, only clay content in volcanic rocks. Increased salinity also cannot explain the single-digit resistivities; a salinity of 4000 ppm is required to have a 10 Ωm resistivity at a temperature of 150°C and 30% porosity, which is over 4 four times higher than any chloride concentration measured anywhere within the park.

3.4 Lithology and 2-D Resistivity Profiles

To determine the effects of lithology on resistivity in active hydrothermal zones in Yellowstone, we project drillhole and lithologic contacts onto 2-D resistivity profiles from the airborne EM lines closest to each drillhole. The 1-D EM sounding closest to each drillhole is also calculated and plotted with temperature from White et al. (1975). Each drillhole is between 0 and 80 meters from the nearest sounding. Figures 3.5-3.13 show the temperature, resistivity, and lithologic contacts near drillholes Y-1, -2, -3, -5, -7 and -8, -12, and -13, starting with the southernmost hole, Y-1, and ending with the northernmost hole in Norris Basin, Y-12. Holes C-I, C-II, and Y-9 can be found in the appendix. The locations of each drillhole can be seen in Figure 1.1.

3.4.1 Y-1

Y-1 is located in the Upper Geyser Basin, west of Old Faithful, and is approximately 15 meters southwest of line 33840. Figure 3.5 shows the 2-D resistivity from line 33840 centered around the projections of the Y-1 drillhole. The right panel of Figure 3.5 shows the measured temperatures of Y-1 from White et al. (1975) plotted with the 1-D resistivity of the closest sounding to the drillhole.

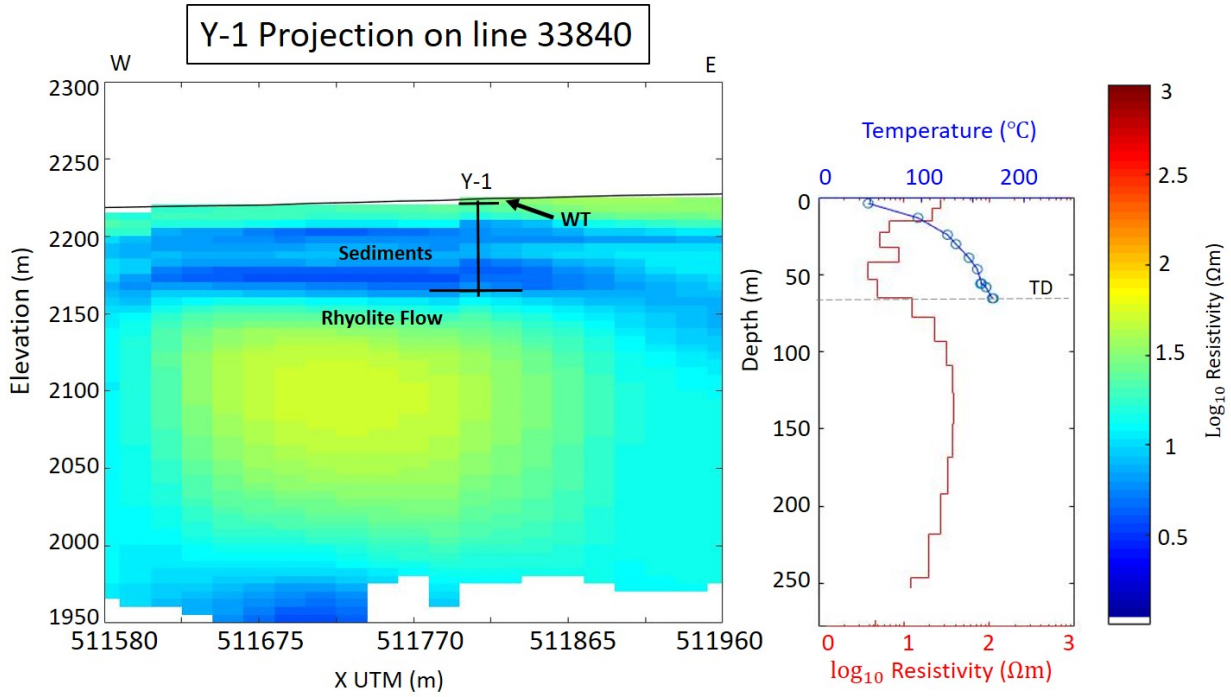

Figure 3.5: Y-1 projected onto 2-D resistivity line 33840. Lithology and temperature from (White et al., 1975)

Y-1 has single-digit resistivities through the majority of the sediment layer, likely indicating high porosity, extensive alteration, and high clay content. The water table within the drillhole, like the majority of the holes, is only a few feet from the surface. It is worth noting that the resolution of the resistivity profile is not fine enough to show the water table near any of the drillholes. The upper 15 meters of the hole have higher resistivities (21 Ωm to

27 Ωm), then transitions to single digits for the remainder of the sediment layer. This is likely due to a higher degree of alteration within the single digit resistivities, which is consistent with Honda's (1970) conclusion that the rocks encountered in Y-1 are heavily altered except for the shallowest levels. Honda (1970) also shows hydrothermal alteration minerals (e.g. mordenite, clinoptilolite, analcime, montmorillonite, and celadonite and various silicas) throughout the hole, with abundant clays from ∼10 meters depth to TD. The presence of clay minerals is consistent with single-digit resistivities encountered below 15 meters within the sediments. A lithologic boundary between the sediments and the underlying rhyolite flow, the Biscuit Basin flow, occurs at approximately 64.5 meters. The total depth (TD) of the hole is 65.6 meters, only one meter into the rhyolite. The lithologic transition from sediment to rhyolite is associated with a resistivity change from single to double digits, which is low considering that rhyolite with 25% porosity at temperatures between 50°C and 200°C has a modeled resistivity over 300 Ωm neglecting clay content (Figure 3.4). Within the Biscuit Basin flow below the TD of Y-1, the resistivity increases from 12 Ωm to nearly 40 Ωm, with lower resistivities at the top of the flow. This suggests a higher degree of alteration concentrated at the top of the flow, but could also be a result of increased porosity or salinity. Temperature increases throughout the extent of the hole from 64°C to 169°C. The resistivities within the sediment layer vary, then increase at the lithologic contact while temperature steadily increases, indicating that lithology contributes to resistivity changes more than temperature in Y-1.

3.4.2 C-1

C-1 is also located in the Upper Geyser Basin, west of Old Faithful, and is 10 meters northeast of line 33840. Similar to Y-1, C-1 has single digit resistivities for the majority of the sediment layer, indicating high porosity and extensive alteration. C-1 transitions

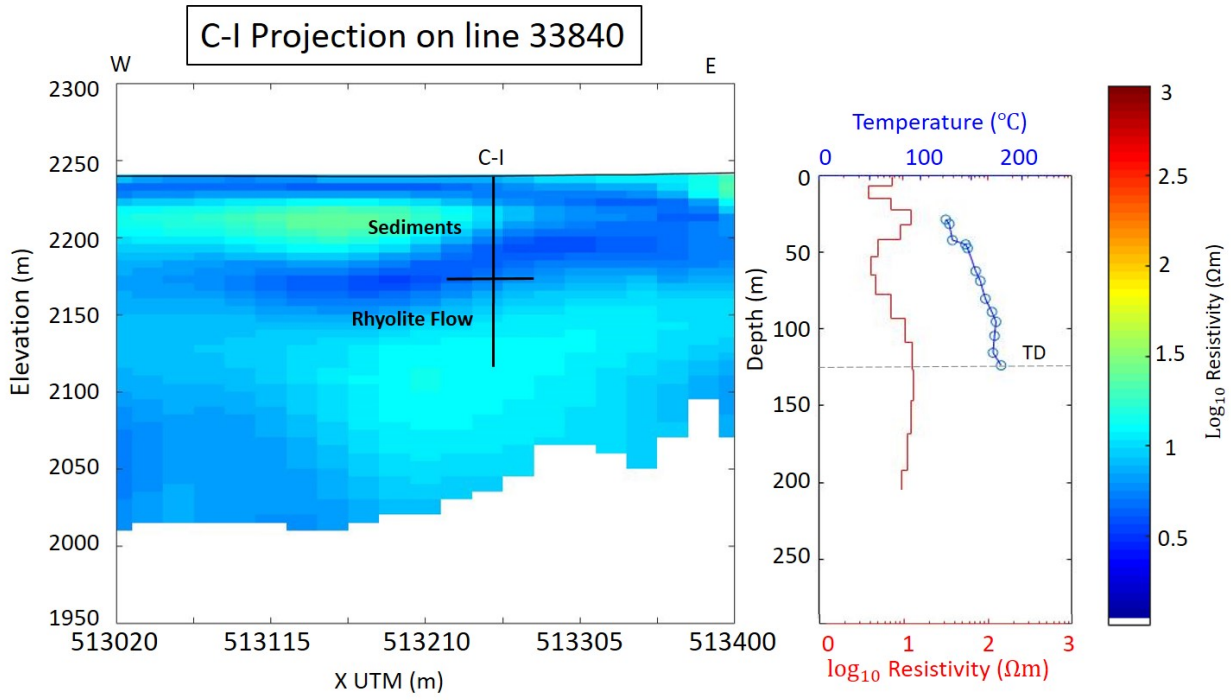

Figure 3.6: C-I projected onto 2-D resistivity line 33840. Lithology and temperature from (White et al., 1975)

from sediments to rhyolite near 67 meters. Similar to Y-1, the transition from sediments to the Biscuit Basin flow occurs at single digit resistivities and steadily increases to 10-20 Ωm with depth. However, the litholigic boundary is defined by a more gradual resistivity transition than Y-1, indicating that resistivity is driven more by alteration than lithology for this hole. The rhyolite resistivities in C-1 are also lower than the rhyolite resistivities beneath Y-1. The TD for C-1 is 123.7 meters, which is well into the Biscuit Basin flow. The measured temperatures for C-1 increase throughout the hole, which does not correlate with the variations of resistivity.

The combination of resistivity and lithology on this line shows that the Biscuit Basin flow in Y-1 and C-1 has a higher resistivity than the overlying sediments. The low resistivities indicate high alteration and clay content within the rhyolite, and more so in the overlying sediments. Although the rhyolite generally has a higher resistivity than the sediments in

both holes, rapid resistivity changes do not correlate directly with litholigic contacts in C-1, suggesting that degree of alteration and clay content affects resistivity more than lithologic contacts. However, the lithologic boundary in Y-1 does correlate with a sharp change in resistivity, which could mean the rhyolite in Y-1 is less altered or less porous than in C-1 making lithology the primary contribution to the resistivity change.

3.4.3 Y-7 and Y-8

Y-7 and Y-8 are the closest drillholes to each other at 130 meters apart. Figure 3.7 shows the Y-7 and Y-8 holes projected onto lines 31350 and 33690, which are 300 meters apart. Y-8 is about 80 meters northeast of the flight line 33690; Y-7 is about 70 meters southwest of line 31350. Given that these are both further from the flight lines than most drillholes, there may be increased error in the interpretation. Both penetrate the Biscuit Basin flow within the northern Upper Geyser Basin, Y-7 at 52.7 meters and Y-8 at 55.2 meters (Keith et al., 1978).

Both profiles show single digit resistivities reaching the surface, although Y-8 penetrates nearly all single-digit resistivities, whereas Y-7 penetrates a more resistive area just outside of the main low resistivity zone. Y-8 is drilled into an upflow zone, and is extensively altered throughout the hole, with the highest alteration within the Biscuit Basin flow from 55.2-62.6 meters (Dobson et al., 2003). At 62.6 meters, the flow transitions to a pumiceous tuff with lower alteration but much higher porosity, averaging 39%, for the remainder of the hole (Keith et al., 1978). The upper 20 meters of the hole has higher resistivities between 10 and 20 Ωm, then decreases to single digits down to the DOI. This could be a result of a combination of lower temperature in the uppermost layer, variable alteration throughout the sediments, and lower porosity within the sediments (about 30%) (Keith et al., 1978). There

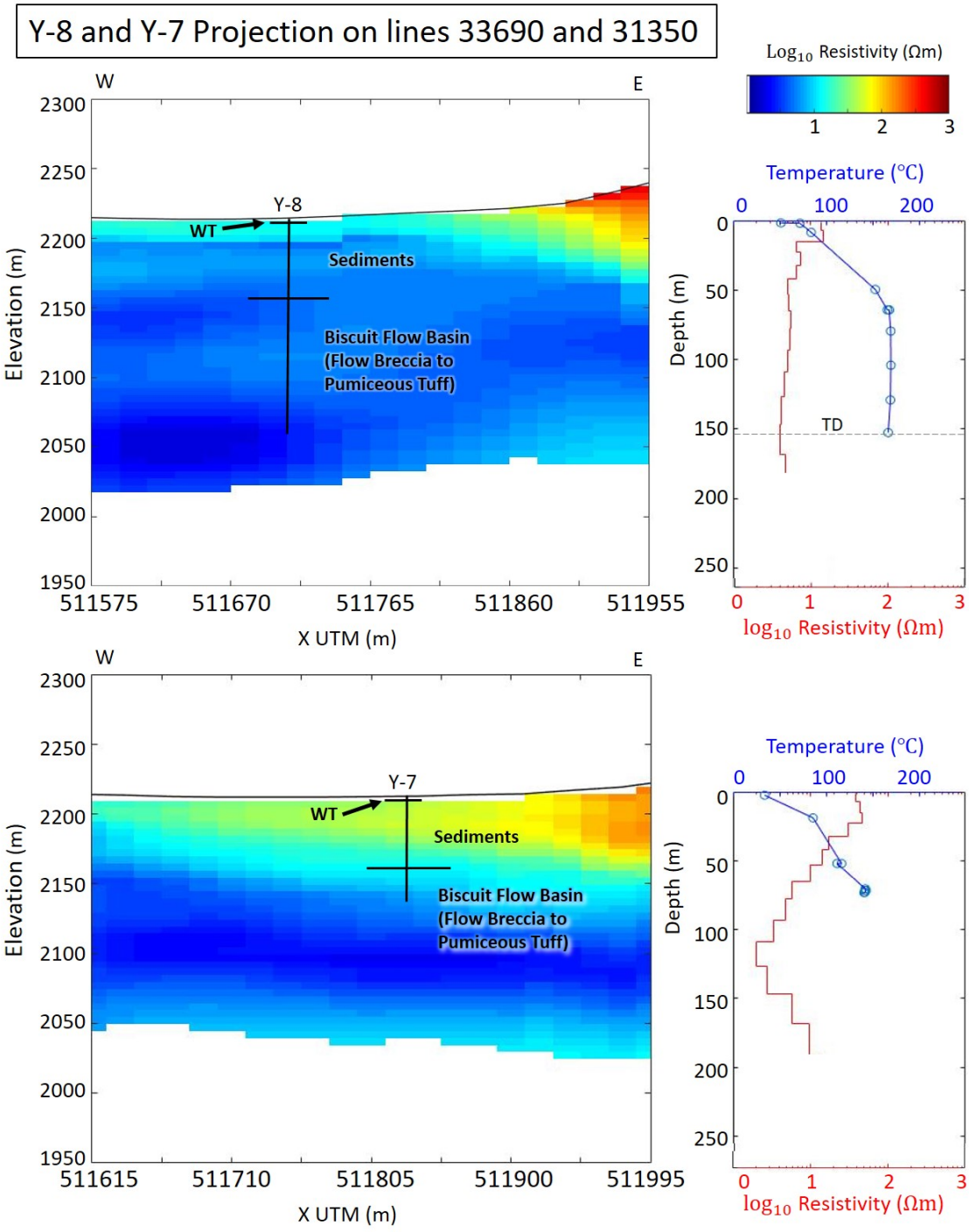

Figure 3.7: Y-7 and Y-8 projected onto 2-D resistivity lines 31350 and 33690. Lithology and temperature from (White et al., 1975)

is no distinct contrast in resistivity at the flow boundary below the sediments, indicating that the resistivity in this area is driven by hydrothermal alteration and conductive clays rather than lithology. Keith et al. (1978) shows that both the Y-7 and Y-8 are altered with more intense alteration in Y-8. The sediments are more altered than the flows, likely due to The principal hydrothermal minerals present in both holes are are clinoptilolite, opal, cristobalite, mordenite, and montmorillonitic clays (Keith et al., 1978). Temperatures in Y-8 are above 150°C from about 50 meters depth to TD, and actually remain constant or decrease slightly below 80 meters. The 1-D resistivity for Y-8 also decreases further into single digits while temperature is stable or decreases.

The Y-7 hole was drilled outside the upflow zone, and there is evidence supporting horizontal self-sealing between the holes (Keith et al., 1978). Y-7, in relation to Y-8, encountered lower wellhead water pressures and down-hole temperatures (White et al., 1975). When projected onto line 31350, the hole lies about 250 meters away from the single resistivities observed at the surface. The resistivity within the sediments ranges between 14 Ωm and 45 Ωm, decreasing with depth. Within the rhyolite, resistivities drop to single digits for the remainder of the hole. This indicates a relationship with the rhyolite and low resistivities outside of a main upflow zone, and may be controlled by the high porosities and alteration within the pumiceous tuff.

3.4.4 Y-5

The Y-5 hole (Figure 3.8) is located in the Midway Geyser Basin near Rabbit Creek, and is about 100 meters southwest of line 31270. The lithologic contact between the overlying sediment layer and the Lava Creek Tuff occurs 9.8 meters below the surface (White et al., 1975). There is no data on the water table for this hole. The sediment layer has resistivities

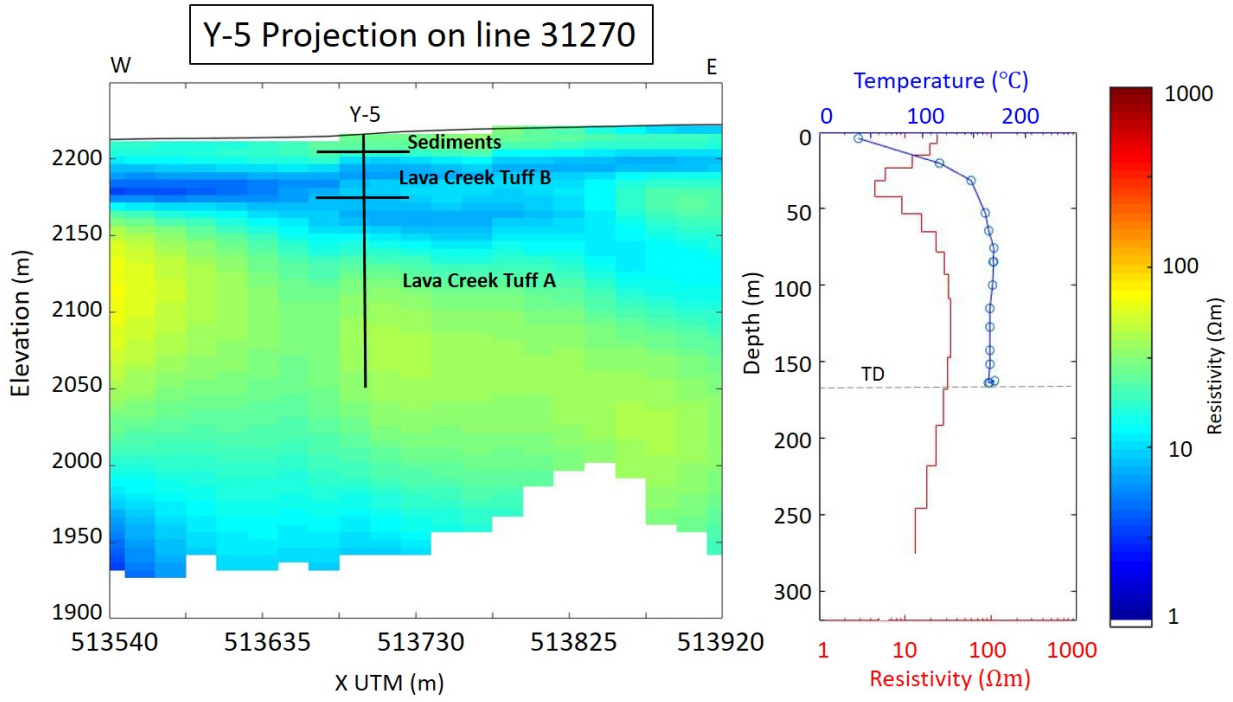

Figure 3.8: Y-5 projected onto 2-D resistivity line 33690. Lithology and temperature from (White et al., 1975)

ranging from 19-23 Ωm, which is higher than the single-digit resistivities in the underlying rhyolite. Within the Lava Creek Tuff, the single-digit resistivities are concentrated in member B and shallow member A, and gradually increase with depth to double digits. This is likely due to the porosity and degree of welding within the tuff. The rhyolitic tuff from the sediment layer to about 45 meters depth is non-welded to weakly welded and has an average porosity of 34.1% (Dobson et al., 2003). Note that the transition from Lava Creek Tuff B to A occurs at 43 meters depth (Keith & Muffler, 1978). The high porosity and weak welding correlate with the single-digit resistivities in the Lava Creek member B. The tuff then transitions to strongly welded tuff with an average porosity of 15.4% (Dobson et al., 2003), and resistivities increase to double digits. In this area, hydrothermal fluids are likely concentrated at the top of the flow due to the higher porosity and weak welding, and spread beneath the sediment layer, and push through at areas such as Grand Prismatic and other nearby hot springs.

Hydrothermal minerals, likely related to the present hot spring regime, occur throughout the Lava Creek Tuff, primarily filling fractures and cavities (Keith & Muffler, 1978). These minerals include chalcedony, montmorillonite, pyrite, mordenite, calcite, and flourite (Keith & Muffler, 1978). The temperatures in Y-5 increase to ∼30 m depth then level out or decrease. The 1-D resistivity is not driven by the temperature change.

3.4.5 Y-2

Figure 3.9 shows the projection of the Y-2 (Firehole Lake) drillhole onto line 33170. The drillhole is about 13 meters northwest of the flight line. Y-2 penetrates two different rhyolite flows: the Elephant Back flow and the Mallard Lake member. Resistivities around the Y-2 hole are generally very low, mostly single digits, and up to 20 Ωm in the sediments. The sediment layer is made up of meters of sinter and travertine to 10.2 meters depth and hydrothermally cemented sand, gravel, and silt to 30.7 meters depth (Bargar & Beeson, 1981). Beds of friable tuff are present from 19.8 to 25 meters and 2.65 to 27.1 meters within the sediment layer(Bargar & Beeson, 1981). The calculated porosities within the sediments layer from 0-30.7 meters depth ranges between 24 and 48% (Bargar & Beeson, 1981). Unlike Y-1, the sediments have a higher resistivity than the underlying rhyolite flow. The Elephant Back flow, which spans depths of 31.7 meters to 122.8 meters in the hole, has single-digit resistivities as low as 4 Ωm and calculated porosities from 5 to 19%, except one layer of pumice and breccia at 66.1 m which has a porosity of 40% (Bargar & Beeson, 1981). The underlying Mallard Lake flow has slightly higher resistivities, up to 16 Ωm, and calculated porosities from 5 to 15% (Bargar & Beeson, 1981). Resistivities beneath the hole (157.4m to TD) decrease with depth as seen on the right panel in Figure 3.9. Temperature and 1-D resistivity of Y-2 show little correlation: temperature increases throughout the hole almost linearly (except at the bottom of the hole, likely due to circulation reversal of drill water

(White et al., 1975)), but resistivity varies, with contrasts near lithologic contacts. Porosity of the different lithologies also doesn't explain the resisivity differences: the sediments have the highest porosities and lower resistivities than the Elephant Back flow.

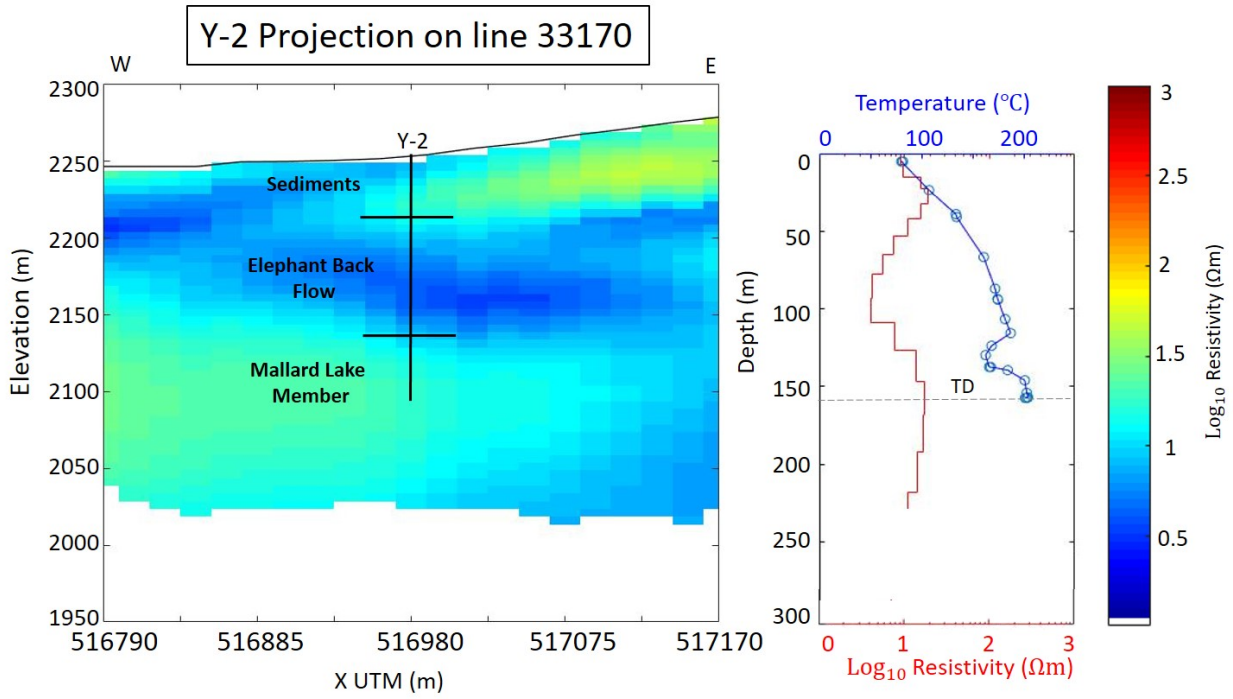

Figure 3.9: Y-2 projected onto 2-D resistivity line 33170. Lithology and temperature from (White et al., 1975)

The lithologic contacts at Y-2 seem to be associated with resistivity contrasts, and the Elephant Back flow has the lowest resistivities. This suggests that the Elephant Back flow has a higher degree of alteration than the underlying Mallard Lake member as well as the overlying sediments. However, when looking at the 2-D profile on either side of the drillhole, resistivities tend to be horizontally compartmentalized, likely due to faults and fracturing more than lithology. About 100 meters west of the hole the sediment layer (if continuous) has a decrease in resistivity and is likely more altered in that zone. According to Bargar & Beeson (1981), hydrothermal alteration throughout the hole is abundant and nearly continuous. Sodium- and potassium-rich clay minerals (e.g. montmorillonite, illite, illite-

montmorillonite, clinoptilolite, mordenite and adularia) are abundant between 56 meters and 102 meters depth, which is within the Elephant Back flow (Bargar & Beeson, 1981). The upper 56 meters contains calcium-rich clays and minerals, but are less abundant than the layer below (Bargar & Beeson, 1981). The remainder of the hole contains sodium- and potassium-rich clays, but less abundant than the zone from 56-102 meters (Bargar & Beeson, 1981). Although not quantitative, the abundance of clay minerals within the 56 to 102 meter zone correlate with the single digit resistivities seen within the elephant back flow. ite

3.4.6 Y-3

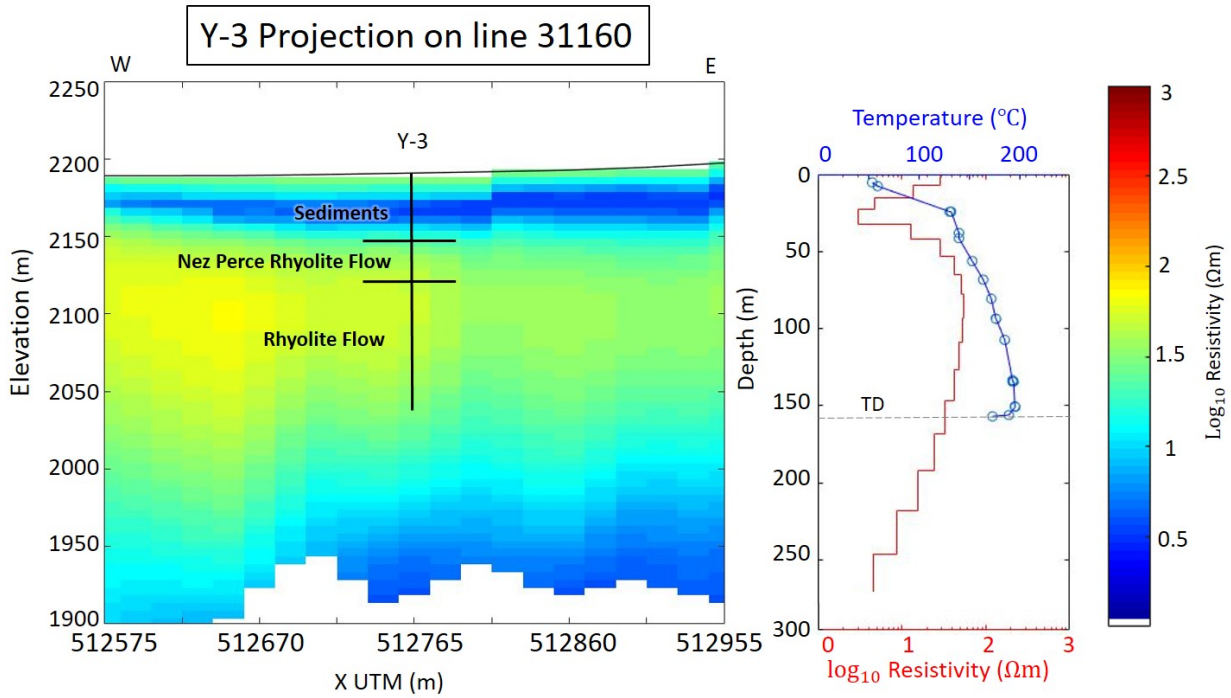

Figure 3.10: Y-3 projected onto 2-D resistivity line 31160. Lithology and temperature from (White et al., 1975)

Figure 3.10 shows the projection of the Y-3 hole onto line 31160. Y-3 is about 13 meters southwest of the flight line. Y-3, like Y-2, also penetrates two rhyolite flows, the Nez Perce

flow from 42.2 meters to 71.3 meters and an unnamed flow beneath it. Y-3 penetrates the edge of a low-resistivity zone that is concentrated at the surface, indicating a higher degree of alteration in the sediments than in the rhyolite. The sediments have a porosities of 15.7 to 45.8% with an average of 35.1% (Bargar & Beeson, 1985). The underlying rhyolite flows have resistivities ranging between 20 Ωm and 60 Ωm, indicating some alteration, fluid saturation and evident porosity, but less than the sediments. The flows have calculated porosities lower than the sediments, ranging from 3.7 to 36.9%, averaging 15.3% (Bargar & Beeson, 1985). Unlike the flows in Y-2, the Nez Perce and unnamed flow don't have an obvious resistivity contrast. However, the lithologic contact between sediments and the Nez Perce Flow is prominent. This could be a result of increased porosity within the sediments, but even high porosity doesn't explain the single digit resistivities. The sediments are likely more hydrothermally altered and contain more conductive clays than the underlying flows. Bargar & Beeson (1985) shows that the Y-3 hole is heavily altered to silicas, zeolites, and clay and mica minerals. The only unaltered obsidian in the hole occurs in the top 10 meters of the hole (Bargar & Beeson, 1985), which correlates with relatively high resistivities. The sediments have a higher concentration of smectite than the flow the flows, and more chlorite and illite-smectite in the flows (Bargar & Beeson, 1985). Since smectite has the highest CEC, it is likely dominating resistivities in the sediments (Revil et al., 1998). Similar to the holes above, temperature alone cannot explain the observed resistivity structure.

3.4.7 Y-13

Y-13 is located in the Lower Geyser Basin, about 60 meters northeast of line 31130. The hole was drilled into an active upflow zone containing highly permeable rocks, surrounded by low discharge springs (White et al., 1975). The lithologic contact from sediment to the Nez Perce flow occurs at 18.6 meters depth, and to a lower unnamed flow (likely Elephant Back

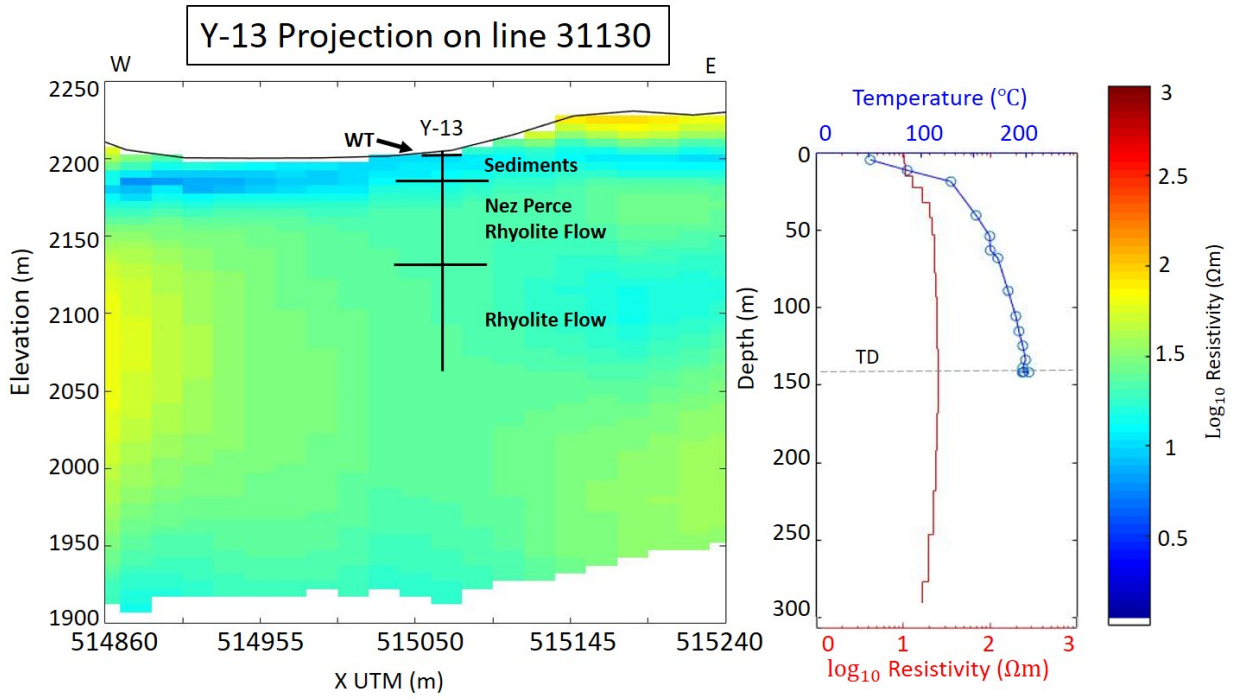

Figure 3.11: Y-13 projected onto 2-D resistivity line 31130. Lithology and temperature from (White et al., 1975)

flow) at 70.1 meters depth (White et al., 1975). The resistivity surrounding the drillhole is lower in the sediments than in either rhyolite flow, and there is no obvious resistivity change between the flows. Temperatures increase from about 50°C to over 200°C within the hole, while the resistivity actually increases. The difference in resistivity between the rhyolite and sediments suggests increased alteration and clay content within the sediments, although the rhyolite must still be thoroughly altered to have resistivities between 20 Ωm and 25 Ωm.

3.4.8 Norris Drillholes Y-9, Y-12, and C-II

The drillholes Y-9, Y-12, and C-II were drilled in Norris Basin and penetrate the Lava Creek Tuff members A and B. Norris was chosen for research drilling due to its diverse activity, despite the fact that Norris experiences higher subsurface temperatures and pressures than

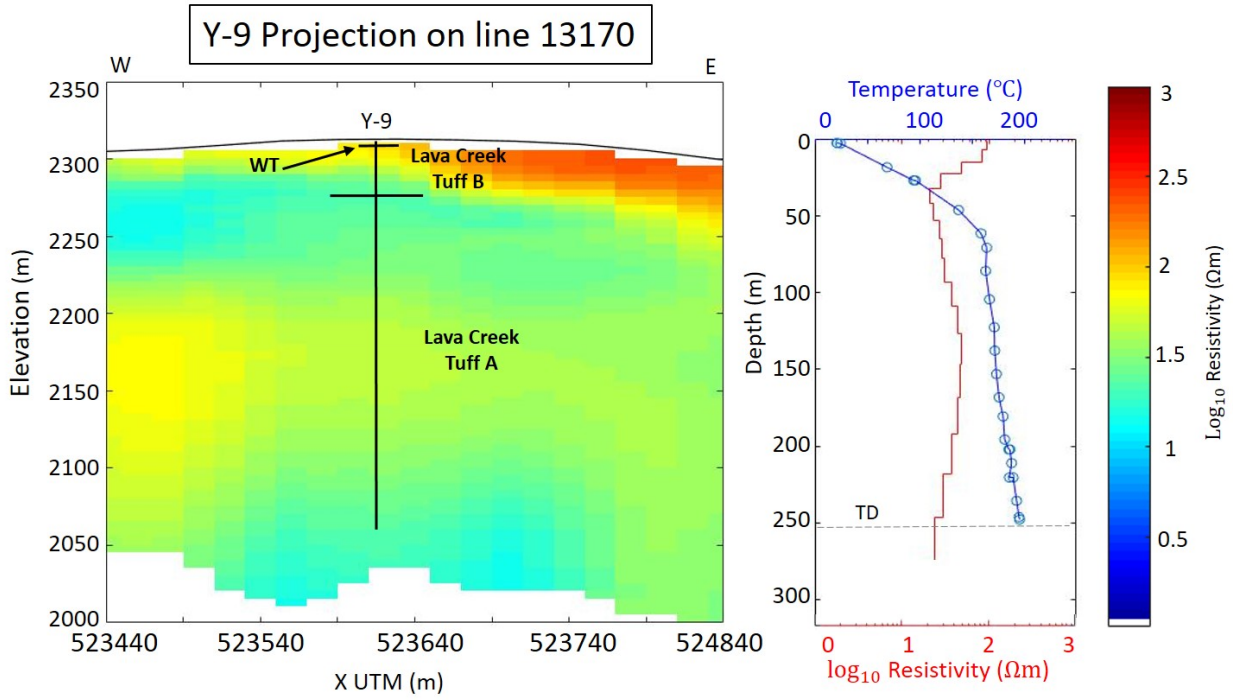

Figure 3.12: Lithology from (White et al., 1975), and 2D resistivity from airborne EM line 13170

elsewhere in the park (White et al., 1975, 1988). Y-9 and Y-12 are the two deepest drillholes in Yellowstone, with TDs of 247.8 meters and 331.6 meters, respectfully. The projections of the Norris drillholes Y-9, Y-12, and C-II onto lines 13170, 13140, and 13160 are shown in Figures 3.12, 3.13, and 3.14. Y-9 is about 35 meters south of line 13170, Y-12 is about 42 meters south of line 13140, and C-II is about 20 meters south of line 13160.

The contact between Lava Creek Tuff members B and A occurs at 37.8 meters in Y-12 as seen in Figure 3.13 (White et al., 1975). The Lava Creek Tuff B is more resistive than member A in each of the Norris drillholes, with resistivities generally over 100 Ωm. These higher resistivities are consistent with modeled resistivities of unaltered to slightly altered volcanic rock with fluid within the pore spaces. Y-12 shows a good correlation with the flow boundary and resistivity decrease from member B to A. Y-9 and C-II show the flow boundary within a lower resistivity, which could indicate a higher degree of alteration and clay content

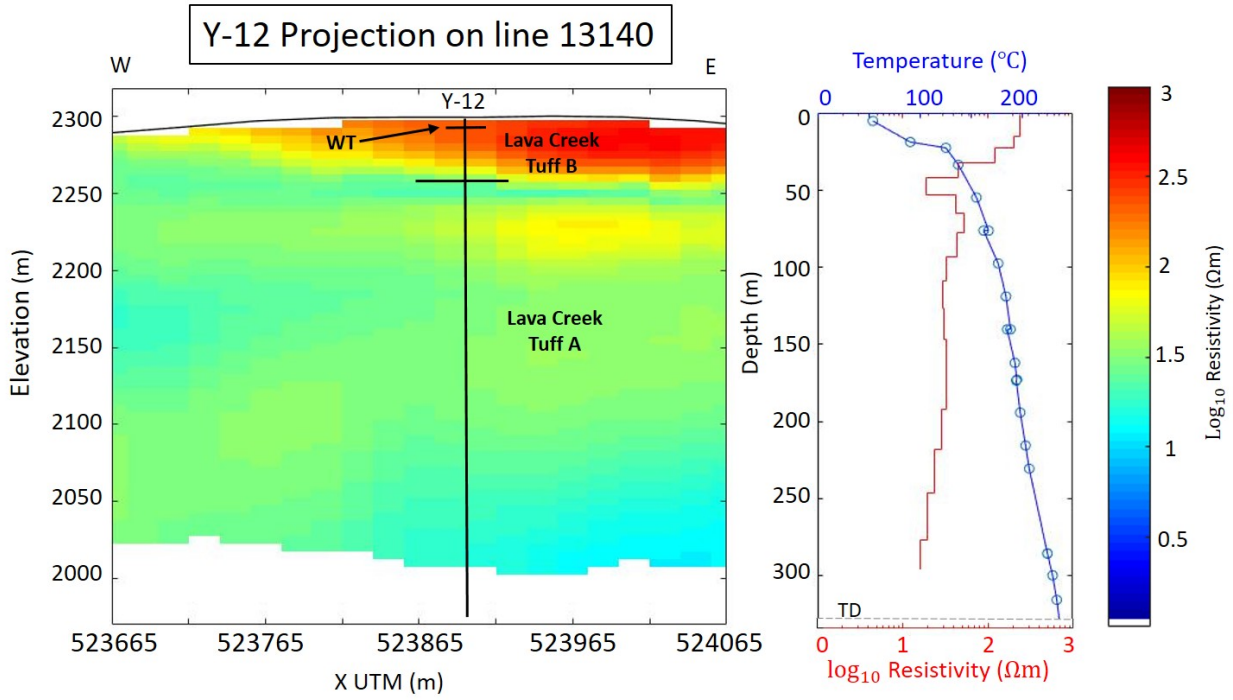

Figure 3.13: Y-12 projected onto 2-D resistivity line 13140. Lithology and temperature from (White et al., 1975)

on the deeper section of member B, or errors from the projection of the holes onto the lines. These projections can be seen in the Appendix. However, it is clear that the Lava creek Tuff member B has consistently higher resistivities than member A, indicating fresh volcanic rock without clays. Since the original rocks of the Lava Creek Tuff are devitrified rhyolitic ash flows, they are less hydrothermally unstable than other flows within the park, specifically glassy tuffs (White et al., 1988). This could explain the higher resistivities (i.e. not single-digit) seen in Norris Basin compared to the hole drilled in other main upflow areas in the park. The hydrothermal alteration minerals present in the Norris drillholes include chalcedony, quartz, pyrite, goethite, kaolinite, montmorillonite, and illite-montmorillonite (White et al., 1988). There is a higher concentration and more variety of clays in Lava Creek Tuff member A than B, aided by higher temperatures increasing with depth (White et al., 1988).

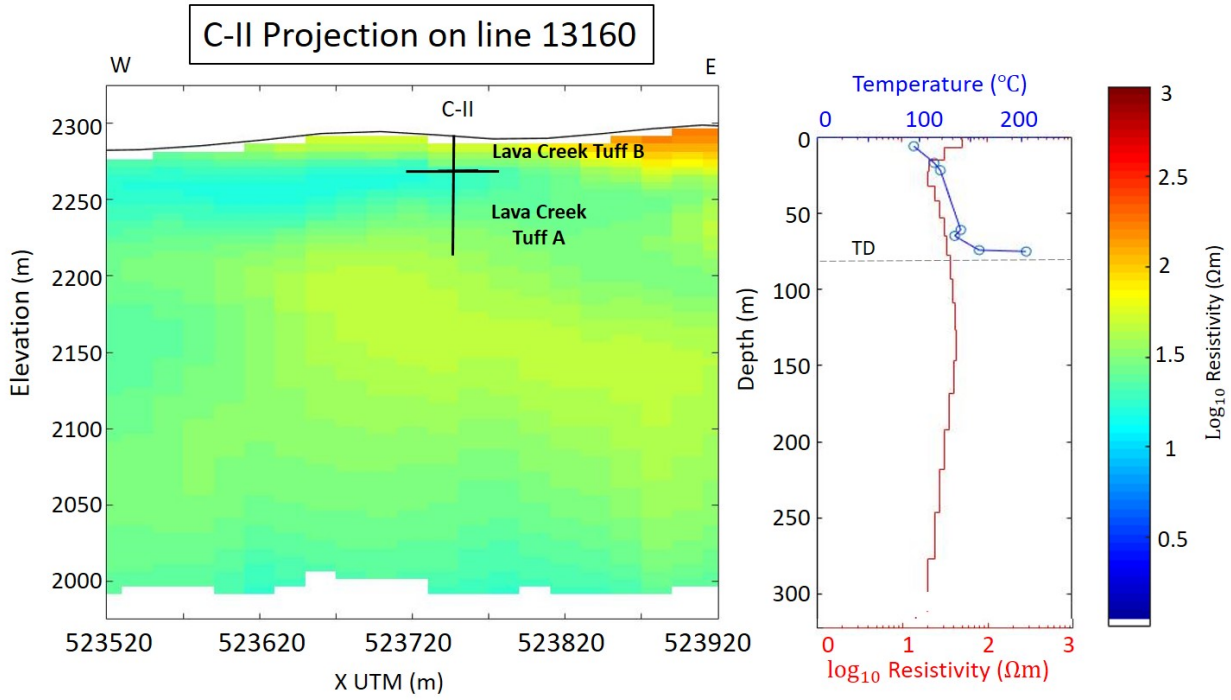

Figure 3.14: Lithology and temperature from (White et al., 1975), and 2D resistivity from airborne EM line 13160

Temperatures in Y-12 approach the reference boiling curve, and are notably high in Y-9 as well. Both Y-9 and Y-12 show a steep temperature gradient in the upper 25 meters, and a shallower gradient for the remainder of the holes. This change in slope occurs near the flow boundary in Y-12, and is more gradual in Y-9. These are some of the highest temperatures recorded in Yellowstone, but resistivities surrounding the holes do not reach single digits as they do in other areas of the park. Therefore, temperature likely does not affect the resistivity to the same degree as clay content and alteration.

Discussion

4.1 Physical controls on resistivity

The drillhole temperatures and resistivities nearest to the drillhole show little correlation. At temperatures between 150°C and 200°C, resistivities range from single digits to nearly 100 Ωm. In comparison to the predicted resistivity of volcanic rock with temperatures ranging from 20°C to 250°C (Figure 3.4), the measured resistivities from the drillholes are much lower. Although electrical conductivity is sensitive to temperature, in hydrothermal areas resistivity is dominated by other factors such as clay content and lithology. This is consistent with findings from Flóvenz et al. (2005), Hersir et al. (2013), and Nono et al. (2018); the resistivities in geothermal systems are dominated by alteration and surface conductivity.

The modeled effects of porosity and temperature of sediments and rhyolites in Yellowstone show higher resistivities than measured values. Resistivities calculated from porosities between 20% and 30% (higher than average for Yellowstone volcanic rock) at high temperature are over 300 Ωm, which is significantly higher than measured values (single- to double- digits). Increased porosity and higher temperatures enhance the hydrothermal alteration process and are therefore associated with low measured resistivities. However, these factors alone do not explain the observed variability of resistivities in Yellowstone, nor do they reach levels that can drive resistivities to the single digits seen in active areas. Salinity of hydrothermal flu-

ids is also unlikely to drive resistivities to single digits given that a salinity of 4000 ppm is needed, which is much higher than measured chloride concentrations anywhere in the park.

Lithologic transitions from sediments to rhyolite and between rhyolite flows have inconsistent effects on resistivity. For most of the drillholes, the resistivity of rhyolites varies between 10 Ωm and 50 Ωm, sometimes even reaching single digit resistivities. Generally these rhyolites have porosities near 20%; however, volcanic rock such as pumiceous tuff have very high porosities (over 50%), which contributes to the low resistivity (Dobson et al., 2003). It is worthwhile to note that fresh volcanic rock without fluid-filled pore space has a resistivity of 5,000 Ωm or more and is drastically lowered by even a few percent of water filling the pore space (Finn et al., 2007, 2018). On the other hand, dry, altered volcanic rocks have resistivities from 100-850 Ωm (Finn et al., 2007). Therefore, in order to achieve single- and double-digit resistivities in a rhyolite flow or tuff, there are likely hydrothermal fluids and clays.

Each altered rhyolite flow exhibits differences in resistivity. Rhyolite flows such as the Elephant Back flow and Biscuit Basin flow have single-digit resistivities, whereas the Nez Perce and Mallard Lake member have resistivities ranging from 10 Ωm to 50 Ωm. In holes such as Y-1 and Y-5, lower resistivities are concentrated at the top of the flows near the lithologic transition to sediments, and gradually increase with depth. On the contrary, in Norris there is a direct relationship with higher resistivities within the Lava Creek Tuff member B than the underlying member A. The inconsistent correlation between lithology and resistivity across multiple flows indicates that resistivity within the rhyolites is dominated by clays and alteration more than lithology.

There is also variability in resistivity changes across lithologic boundaries. Drillholes such as Y-2, Y-5, Y-7, show lower resistivity values in the rhyolite flows than in the overlying sediments. The sediment layer generally has a higher porosity than the rhyolite (with the

exception of pumiceous tuff), and temperature does not correlate well with resistivities, indicating that the volcanic rock must be more altered and have a higher CEC than the overlying sediment since its resistivity is lower.

In contrast, the resistivities of Y-1, Y-3 and Y-13 show that the overlying sediments are more conductive than the rhyolite flows beneath them, which have characteristic 10 Ωm to 50 Ωm resistivities. In these areas, the sediments may have a higher degree of alteration and CEC than sediments in areas surrounding the other drillholes, as well as the underlying volcanic rock. In these cases, it is also likely that alteration and fluid movement is concentrated within the sediments.

Holes Y-2, Y-3, Y-13, and Y-12 (and C-II and Y-9) penetrate two separate rhyolite flows. In the case of the Norris holes, which go through Lava Creek Tuff member B then member A, the overlying member B has a higher resistivity, much closer to the values we see for rhyolites in inactive zones of Yellowstone. Similarly, in Y-2 there is also a resistivity contrast between the Elephant Back Flow, which has single digit resistivities, and the Mallard Lake Member, which has resistivities between 10 and 30 Ωm. However, in Y-13 and Y-3, the Nez Perce flow and underlying unnamed flow do not have any contrast in resistivity.

In hole Y-8, lithology doesn't seem to contribute as much to the change in resistivity. Y-8 shows single digit resistivities for the majority of the hole, and no change over the lithologic contact between sediments and volcanic rock. This is likely due to the severe alteration throughout the hole, which dominates the resistivity. This correlation is also seen in the 2-D resistivity lines 11660 and 33690 (Figures 3.1 and 3.2). The mapped geothermal alteration from White et al. (1975, 1988), Keith et al. (1978); Keith & Muffler (1978), and Bargar & Beeson (1981) correlates with the low resistivity zone, not with rhyolite flow boundaries. The complex relationship between lithology and resistivity indicates that while lithology affects resistivity, in highly altered areas, resistivity is dominated by clays and alteration more than

lithology.

4.2 Applications

In this thesis we investigate the controls on electrical resistivities in hydrothermal areas in Yellowstone. The properties tested are fluid saturation, porosity, temperature, salinity, and clay content. Using rock physics and correlations between resistivities and drillhole data, we find that clay content must be present to to have single-digit resistivities in Yellowstone. Hydrothermal alteration driven by rock-fluid-gas interactions fills void space and replaces volcanic glass with silicas, clays, and zeolites (Honda, 1970). Since clays are electrically conductive, the low resistivities seen in Yellowstone are essentially mapping clays deposited during hydrothermal alteration. This information will let us interpret resistivities in Yellowstone from the entire airborne EM survey. Low resistivity zones must be either active hydrothermal areas that are hot and contain hydrothermal fluids and minerals, or fossil hydrothermal areas that contain the remnants of clay from past alteration. Since resistivity contrasts also correlate with lithologic contacts, the airborne EM data can be used to map rhyolite flows and the depths of glacial sediments in hydrothermal areas. This data also gives insight into hazard assessment within the park. Many resistivity profiles show low resistivities near the surface, but are not mapped geothermal areas and do not show alteration on the surface. These surficial low resistivities could be new old, inactive areas that are hydrothermally altered, or they could be new hydrothermal areas that haven't pushed through the surface yet. Identification of low surficial resistivities could limit development of infrastructure (i.e. roads, lodges, boardwalks, etc.) in potentially hazardous areas.

The next steps for the EM data include correlating the EM and magnetic data with surficial and bedrock geology to understand the fracture system in Yellowstone in relation to

hydrothermal alteration. This will aid in the analysis of subsurface structures that guide deep, hot fluids to the surface. The EM and magnetic data can also be used to delineate flow boundaries and distinguish lithologic controls on hydrothermal pathways.

Although this study does not include quantitative clay content effects on resistivity, further research can be done relating the clay content and type from the drillholes with resistivity. Studies discussing the alteration within Yellowstone drillholes (i.e. Bargar & Beeson (1981, 1985); Keith & Muffler (1978); Keith et al. (1978); Honda (1970)) show relative amounts of clays and hydrothermal minerals, but do not show quantitative values. Each hole also contains a variety of clay types, each with different CEC values; therefore each clay decreases resistivity by a different magnitude (e.g. a rock altered to smectite can decrease resistivity up to 10 times lower than a rock altered to illite (Ussher et al., 2000)). A quantitative analysis of clays in Yellowstone will further constrain resistivity interpretations.

Conclusion

The combination of temperature, porosity, alteration and clay content, lithology, and salinity make investigating resistivities in Yellowstone very complex. Some lithologic contacts correlate with resistive transitions, and some do not. Although the overlying sediment layer is often more porous than the volcanic rock, resistivities were not consistently lower in the sediments than the flows. Drillhole temperatures and associated 1-D resistivities do not correlate well, which suggests that temperature, at least to the first order, does not control resistivity. Therefore, although increased temperature and porosity decrease resistivity, their contribution is not substantial enough to account for single digit resistivities. Single digit resistivities in Yellowstone's upper 300 meters must contain clay and extensive hydrothermal alteration which contribute to the surface conductance of the rock. We conclude that resistivities in Yellowstone are controlled mainly by water saturation, clay content, and hydrothermal alteration, with variable dependence on lithology, and are not dominated by temperature.

Appendix A

6.1 1D Resistivity and Lithology for Drillholes

Borehole temperature and lithology compared to resistivity

To determine the effects of lithology and temperature on resistivity in active geothermal zones in Yellowstone, we compare the lithology and temperature of the borehole data with the resistivity soundings from the airborne EM data in borehole locations. Figure 6.1 shows nine of the drill holes plotted by 1-D resistivity and lithology. Resistivity data is from the LCI of the airborne EM survey and is the nearest sounding to the actual borehole. The plots are color coded by lithology, with reds and oranges signifying rhyolite flows and blue and black representing sediments and sinter. The codes used to generate these plots can be found in section 8.1.4.

6.2 Electrical Conductivity and Hydrothermal Areas

Electrical conductivity is sensitive to changes in temperature, pressure, water content, clay content and salinity, making it a useful property when characterizing hydrothermally altered areas. Although there is minimal salinity in this area (Nordstrom et al., 2009), the

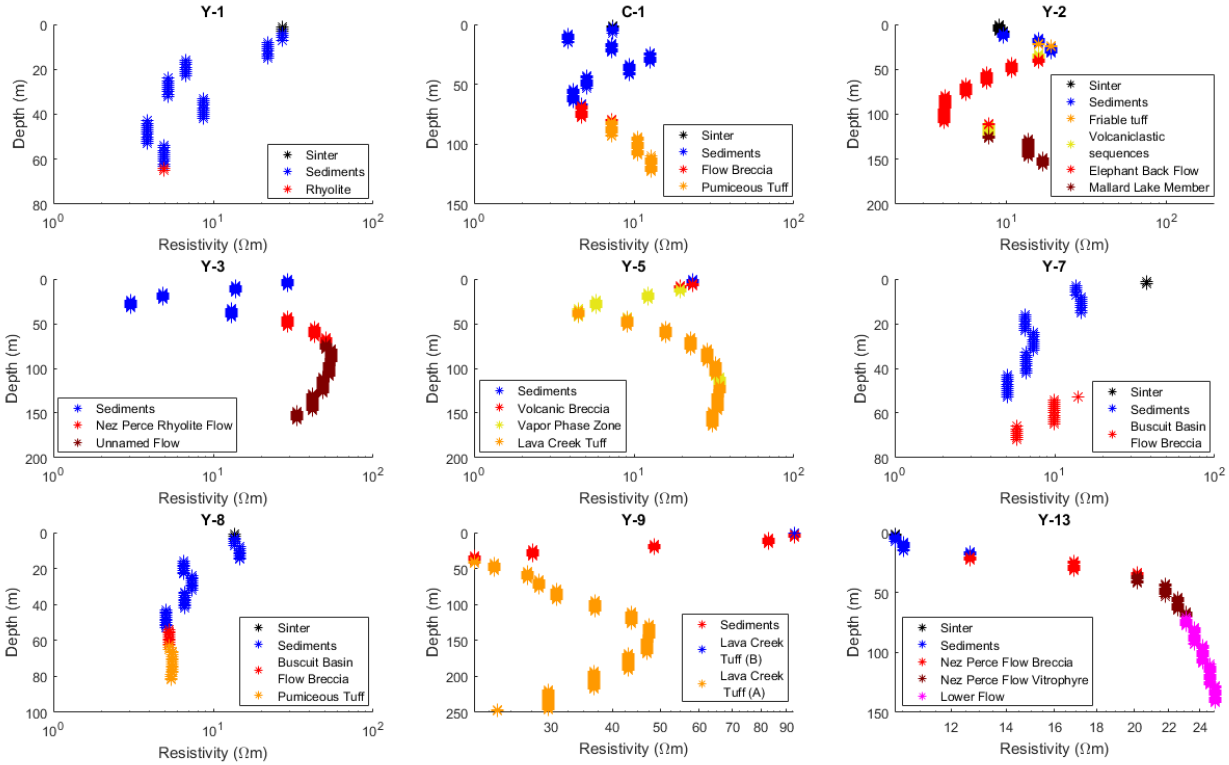

Figure 6.1: Lithology from White, 1975, and resistivity from airborne EM for nine holes drilled in Yellowstone.

other factors are dominant in the Yellowstone hydrothermal system. Cooler colors (blue) represent conductive zones and hot colors (red) show resistive zones. The resistive zones are predominantly dry rhyolite flows. Active hydrothermal zones and hydrothermally altered areas contain variations of higher pressure and temperature, increased clay content, and/or fluids whereas inactive zones generally do not. Therefore, we conclude that robust changes in resistivity show boundaries between inactive areas and hydrothermally altered areas, but do not distinguish active pathways from paleopathways within the hydrothermally altered zones.

As stated above, higher electrical conductivity is associated with hydrothermally altered and active zones in geothermal areas, making it an ideal property to use when studying geother-

mal systems. A comparison of 1D soundings representative of both hydrothermal zones and non-hydrothermal zones in Yellowstone is shown in Figure 6.2. In general, unaltered areas have characteristically high resistivities, often above 1000 Ωm, and have a deeper depth of investigation nearing 600 meters. The resistivities in these zones show a decrease in resistivity with depth of about 10 times from the surface to 600 meters in depth. This is likely due to an increase in temperature with depth, and possibly increased fluid saturation. Hydrothermal zones typically have surface resistivities around 100 Ωm and fluctuate down to single digits at variable depths. These areas also have a more shallow depth of investigation due to the diffusive nature of the EM fields. The geographic locations and sounding placements for each zone can be found in Appendix 1. Each area is made up of 144 1D soundings from the SCI inversion and have been plotted with depth. There is a clear gap between the hydrothermal areas and the non-hydrothermal areas, thus reiterating that resistivity is a suitable property to distinguish hydrothermal from non-hydrothermal areas.

6.3 Resistivity in Hydrothermal and Non-Hydrothermal Areas

Figure 6.2 showed the resistivity standard deviations of seven areas in Yellowstone, four non-hydrothermal areas and three hydrothermal areas within the Geyser Basins. Each area is made up of 144 (12 x 12) 1D resistivity soundings from the SCI inversion scheme over an area of about 0.3 km^2.The geographic locations for these areas can be seen in Figure 6.3. The layout of the 1D soundings near Old Faithful can be seen in Figure 6.4. The code used to generate this plot and Figure 6.2 can be found in Appendix C.

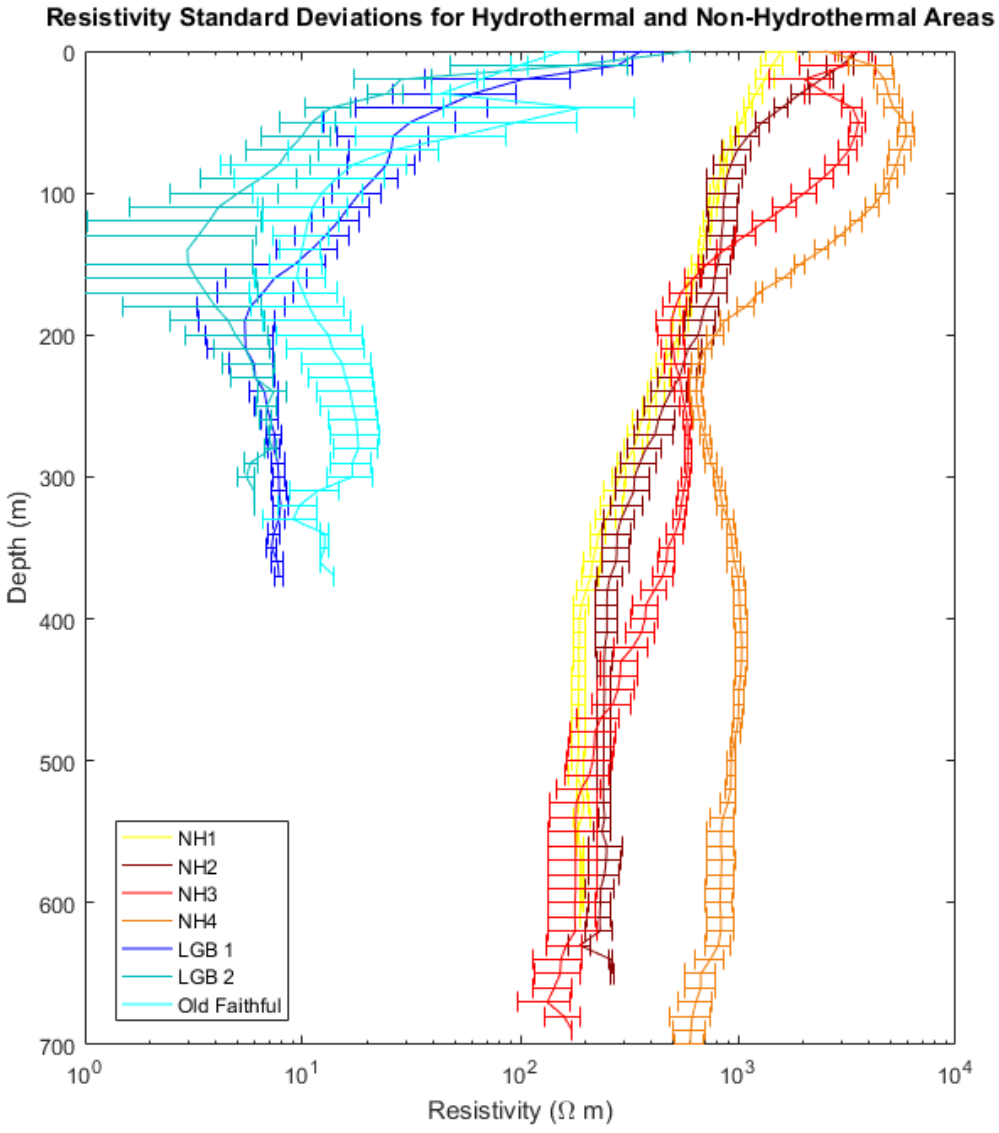

Figure 6.2: Standard deviations of 1D soundings from representative hydrothermal (Lower Geyser Basin 1 and 2, Old Faithful) and non-hydrothermal (Non-Hydrothermal 1-5) areas in Yellowstone. Each area is made up of 144 (12x12) soundings spaced about 50 meters apart covering a total area of approximately 0.3 km^2.

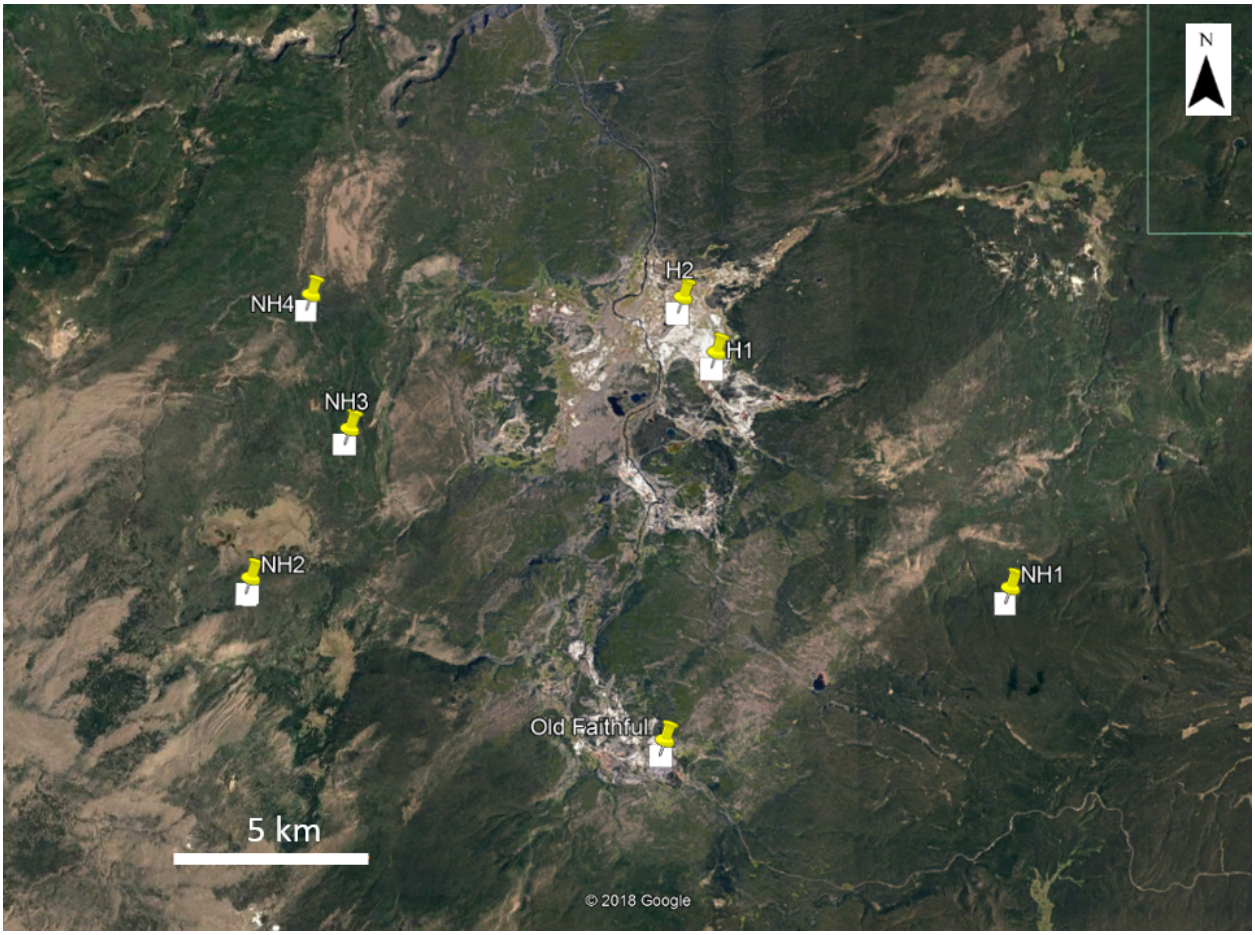

Figure 6.3: Sounding Areas

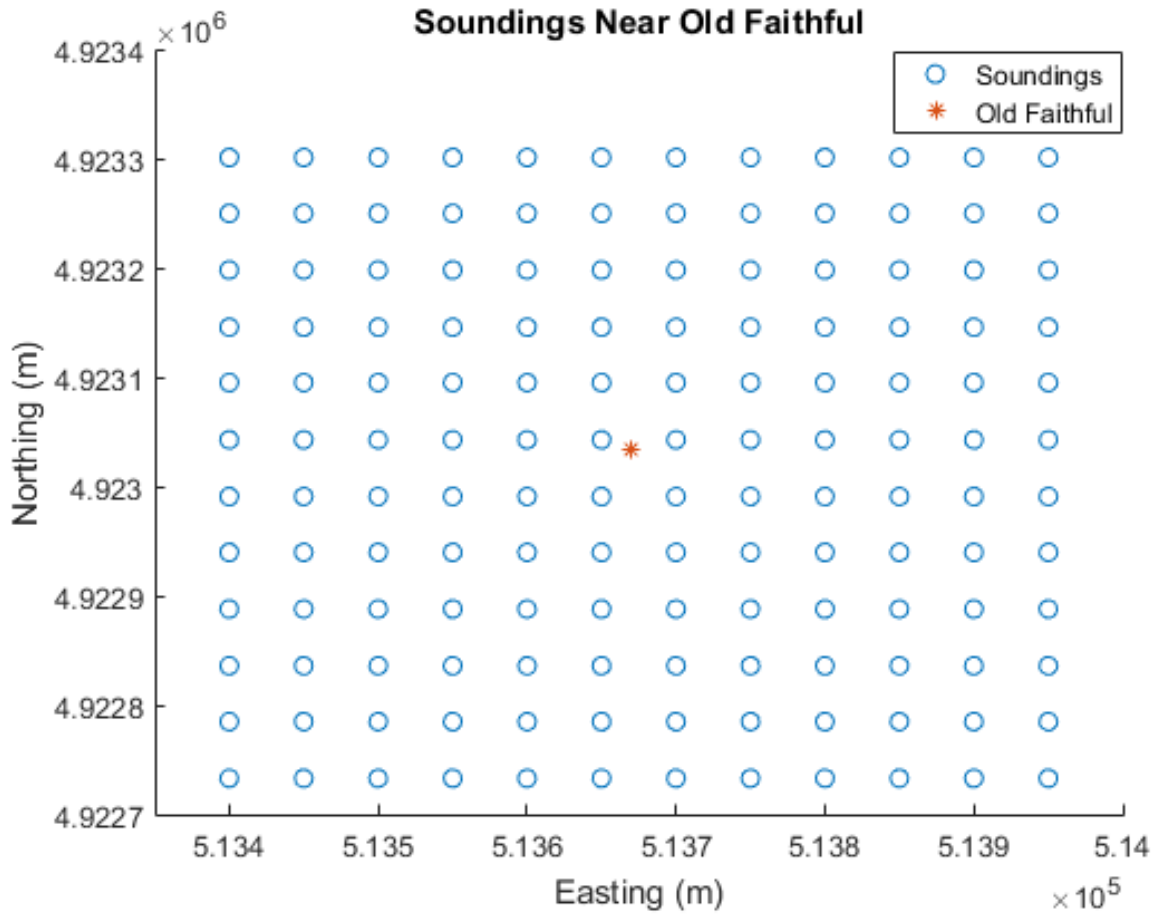

Figure 6.4: Sounding locations around Old Faithful spaced 50 meters horizontally and 51.6833 meters vertically from SCI inversion.

6.4 Joint Em and Aeromagnetics

6.4.1 Comparison with Upward Continued Magnetic data and Resistivity Depth Slice

Aeromagnetic data from Finn & Morgan (2002) and Bouligand et al. (2014) correlate hydrothermally altered areas with magnetic lows in Yellowstone. Since the EM method shows resistive lows in hydrothermal areas, the magnetic data and resistivity data should correlate and distinguish hydrothermal areas if the physical properties contributing to resistive lows are also contributing to magnetic lows. To test this, we processed the magnetic data using a range of upward continuations every 100 meters from 0 meters to 2000 meters and compared it correlated each with a range of resistivity depth slices over the same area. Upward continuation is a filtering technique applied to magnetic data that limits the high frequency responses from surficial geology and focuses on the deep, dominant magnetic trend. Information on the upward continuation process can be found in section 7.2.8. The resistivity depth slices come from the SCI scheme and were calculated every 10 meters for the first 100 meters depth, then every 20 meters until the maximum depth of 600 meters. Each depth slice was correlated with every upward continuation until the best correlation was found.

There is a direct relationship between the upward continued magnetic data and average resistivity depth slices in the Norris Basin. Figure 6.6 shows the resistivity depth slice between 340 and 360 meters (a) and the upward continued magnetic field over the same area (b). Notice the linear hourglass shaped magnetic low zone (b) correlating with the similar shaped conductive zone (a). This correlation shows that hydrothermal alteration, while lowering resistivity due do clay content, temperature, and fluids also affects the magnetic properties of the rock. Since the magnetic properties are not dependent of pressure or

temperature (below the Curie point), the alteration process is likely the cause of the low magnetic anomaly in hydrothermal areas. This is consistent with results from Finn & Morgan (2002); Finn et al. (2007, 2018) who show that alteration shows up in the magnetic data (of the alteration is thick enough), whereas other factors that lower resistivity (e.g. water saturation, temperature, etc.) do not.

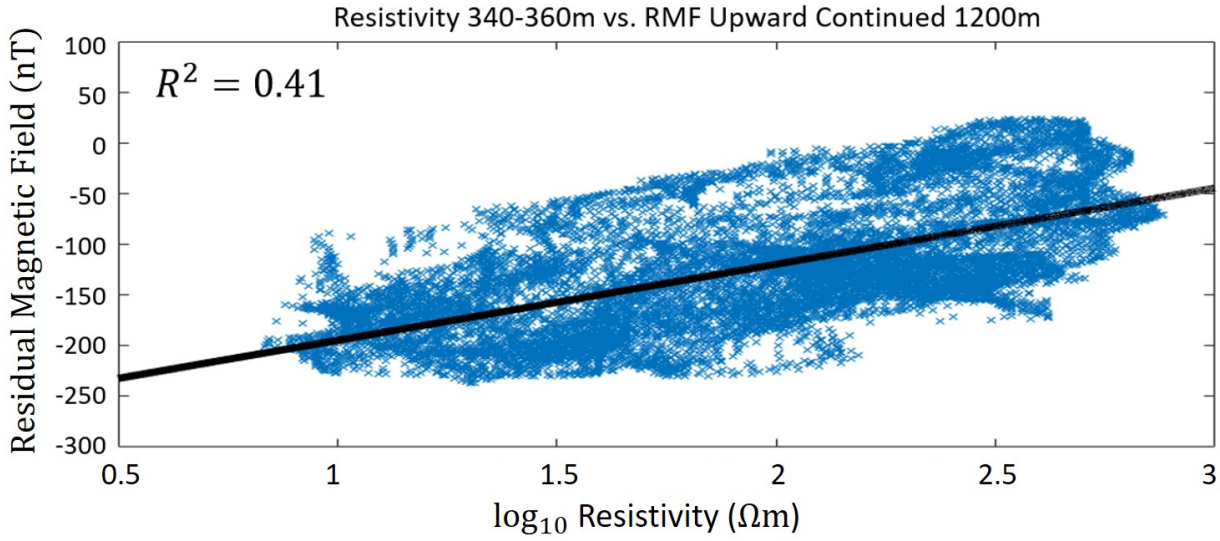

Figure 6.5: Correlation between average resistivity at 340 - 360 meters and residual magnetic field upward continued by 1200 meters for the Norris Basin

The best correlation between the upward continued magnetic field and the average resistivity depth slice occurs at an upward continuation of 1200 meters and an average depth slice between 340 and 360 meters. This correlation has an R^2 value of 0.41 as shown in Figure 6.5. Since the resistive lows and magnetic lows both distinguish hydrothermal areas, we can conclude that the physical properties of the rock that make it conductive and non-magnetic are due to the hydrothermal alteration process. Since magnetic susceptibility is not affected directly by temperature, a magnetic low and resistive low in the same area would show that the decreased resistivity is due to fluids and clay content rather than temperature.

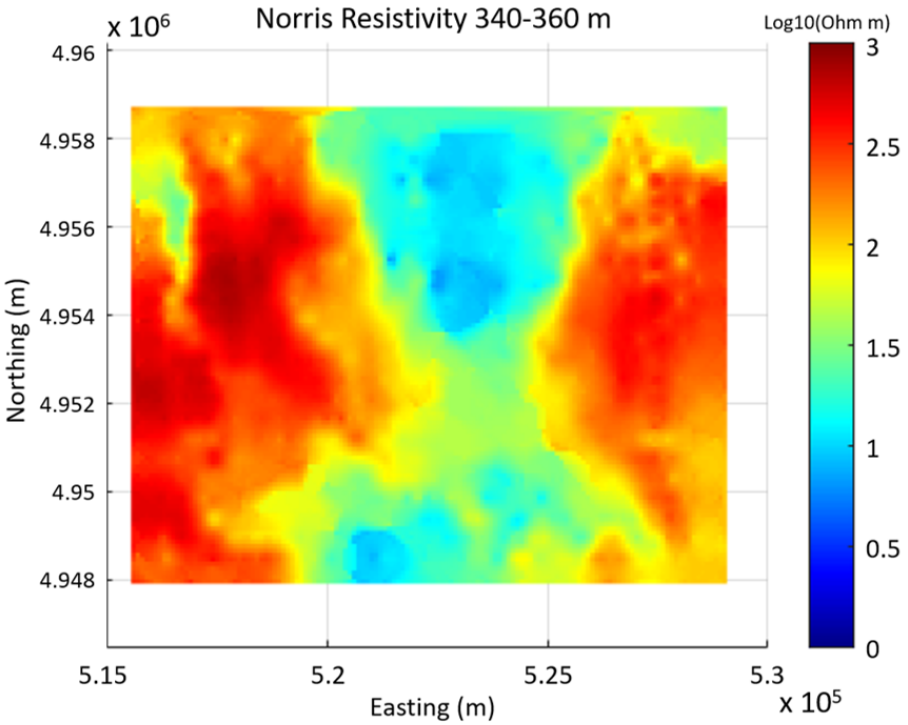

(a) Norris Basin average resistivity from 340 to 360 meters

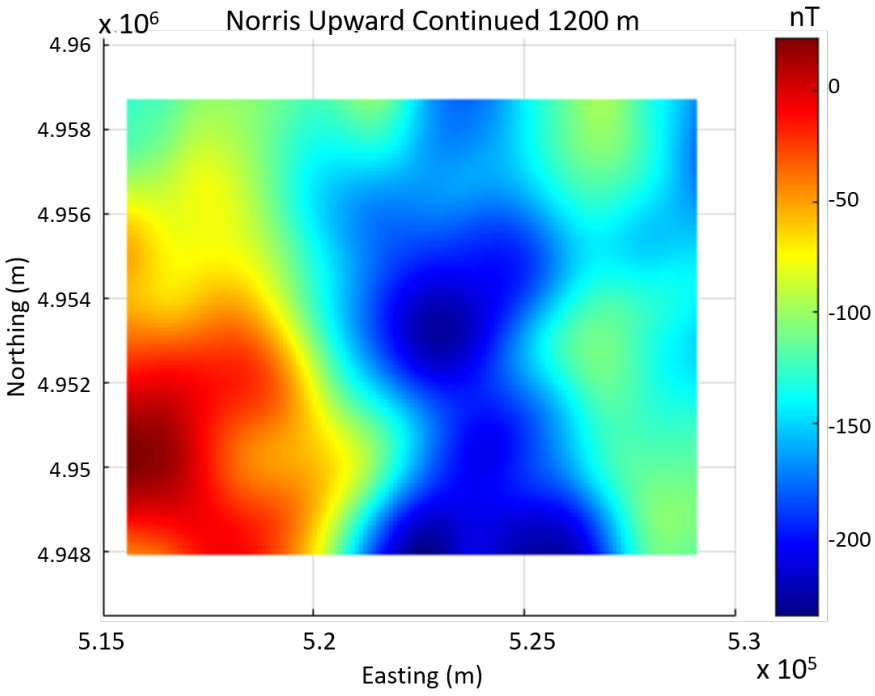

(b) Norris Basin residual magnetic field upward continued 1200 meters

Figure 6.6: Norris average resistivity (a) and upward continued magnetic field (b)

Appendix B

7.1 SkyTEM Survey

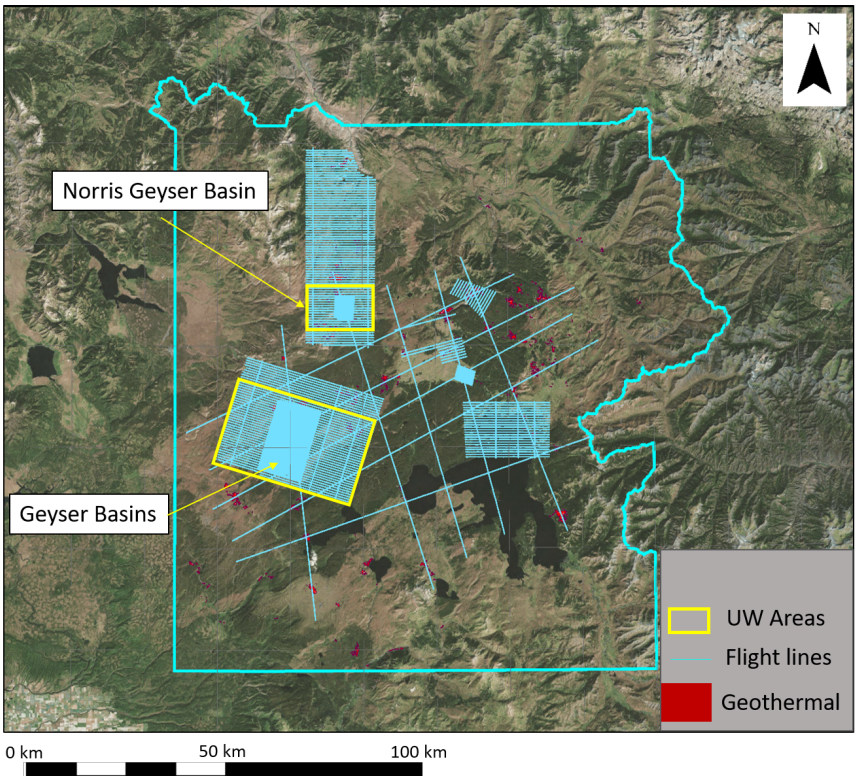

Figure 7.1: Survey lines over Yellowstone with University of Wyoming areas highlighted

Figure 7.1 shows all the acquired survey lines over Yellowstone National Park. Figure 7.2 shows the specific Upper Geyser Basin and Norris Basin survey lines, some of which were

used in this paper.

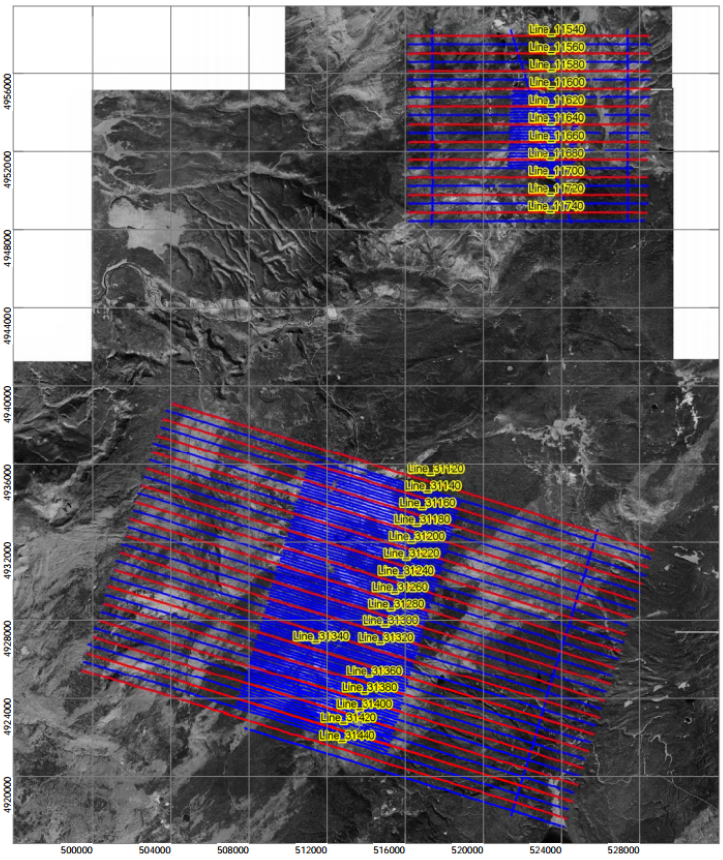

Figure 7.2: Geyser Basins and Norris Basin survey lines

7.2 Data Processing

7.2.1 Airborne TEM

The airborne TEM data was processed using Aarhus Workbench using the *Guide for processing and inversion of SkyTEM data in the Aarhus Workbench*. The SCI inversions were performed by the HydroGeophysics Group, and the LCI inversions for the Geyser Basins and Norris Basin were performed by the author. This section outlines a brief explanation of the SkyTEM processing used for this thesis.

7.2.2 Data Import

The SkyTEM data is imported into the Workbench software as raw data. The following files are imported:

- Geometry file - contains information on the SkyTEM system
- SPS-files - contains GPS, altitude, tilt angle, and transmitter data
- SKB-files - contains the dB/dt SkyTEM data
- Line number file - contains the line numbers and production intervals

7.2.3 Preliminary Processing

The initial processing of the SkyTEM data comprised of reviewing the raw data and manually processing altitude and GPS data. The altitude is the distance between the transmitter coil and the ground, and is measured by two laser altimeters. Altitude corrections are necessary

to remove reflections that do not come from the ground, such as trees. An example of altitude processing can be seen in Figure 7.3.

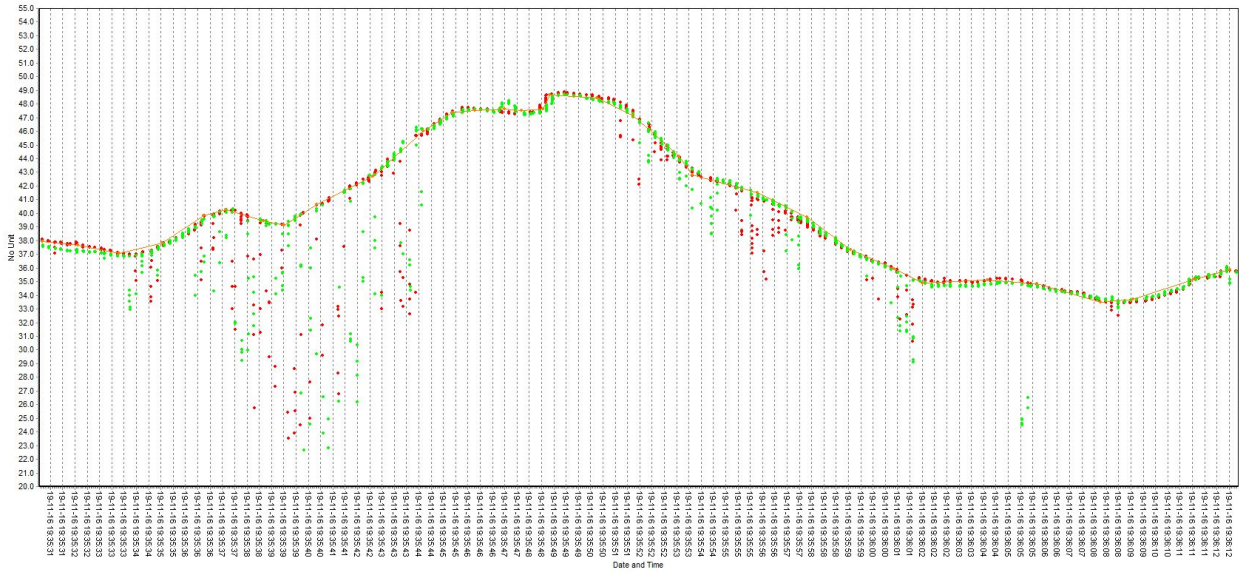

Figure 7.3: Example of altitude corrections. Red and green represent the two laser altimeters, orange represents the corrected altitude. The length is about 1 km. Image is taken from the manual processing of the SkyTEM data in Workbench. The red and green measurements that seem to be noisy and are much lower in altitude than the apparent topography show treetop measurements

7.2.4 Automatic Processing

After making altitude corrections, the SkyTEM data was automatically processed. Automatic processing includes automatic filters, averaging, etc. and includes no manual processing. This is a good first look at the data, but requires manual processing to edit out noise and coupling.

7.2.5 Manual Processing

Manual processing of the raw data is applied after the automatic processing to take out coupled or noise influenced data and high frequency noise. This can be done in a couple ways. The first is to view the raw high moment and low moment data from the time gates, as seen in Figure 7.4. The coupled data is manually removed. Individual time gates can also be removed if they are coupled or contain noise. Time gates 1-8 were removed for all inversions for this reason. This occurred often with time gates 9 and 10, but were edited manually.

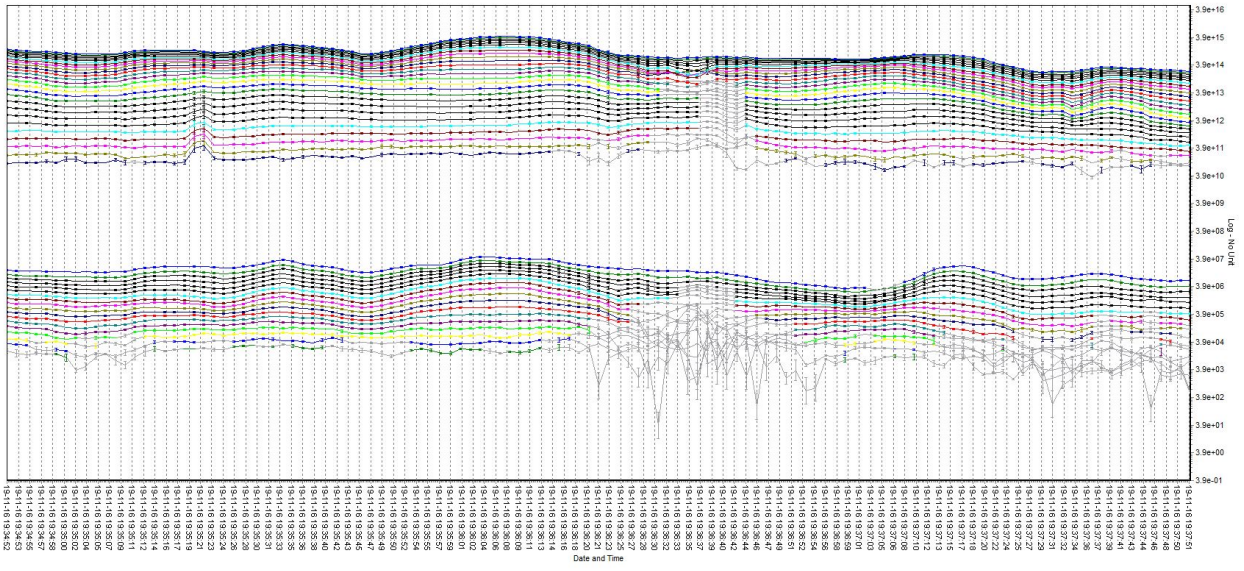

Figure 7.4: Example of manual correction of the averaged HM and LM data. The coupled and noisy data is manually muted (grey). Colored raw data shows time gates for high and low moment data.

Another way to manually process the SkyTEM data is by looking at the sounding curves that show the raw -dB/dt or rhoa high and low moment data. Any coupling is manually removed such that the sounding curve is smooth. Viewing the soundings is a good way to inspect the manually processed SkyTEM data. Figure 7.6 shows the sounding curve in the processing step, Figure 7.7 shows multiple dB/dt soundings after coupled and noisy data

have been removed.

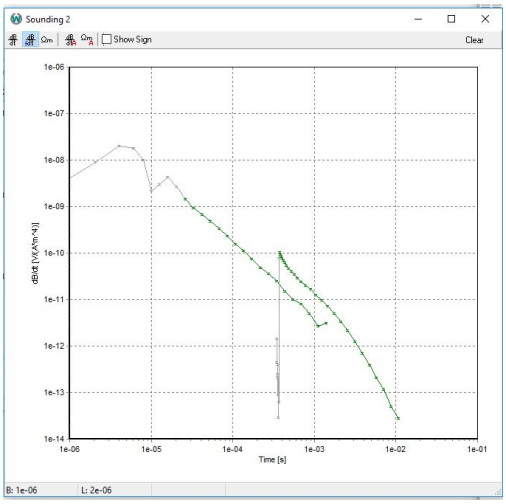

Figure 7.5: Raw dB/dt soundings for high and low moment data with coupled data and early time gates muted

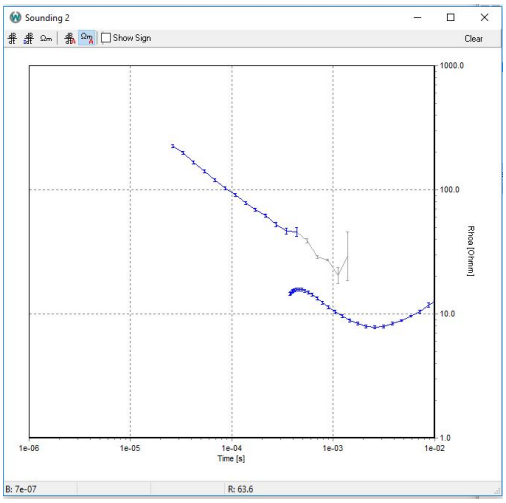

Figure 7.6: Raw rhoa soundings for high and low moment data with coupled data and early time gates muted

After the manual processing is complete, a smooth LCI scheme is applied and visual inspection of the resistivity profile is done. If there are any obvious anomalies, the data is reprocessed and the inversion is run again.

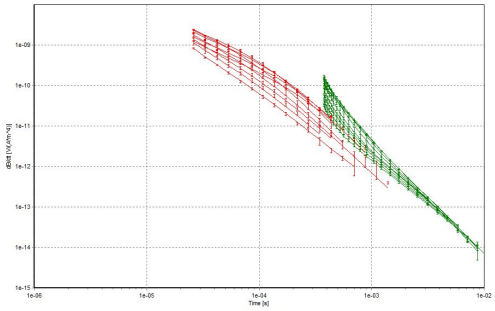

Figure 7.7: Final dB/dt soundings for HM and LM data

7.2.6 Inversion

As discussed in section 2.0.3, an LCI (laterally constrained inversion) scheme was used which inverts single resistivity lines using line data as lateral constraints but does not incorporate data from adjacent lines. Inversions were performed using the Aarhus Workbench software package, specifically the AarhusInv inversion code (Auken et al., 2014). The inversion is a 1-D full non-linear damped least-squares solution which models the transfer function of the instrumentation. I used a 25 layer model and used automatic *a priori* resistivities. Sensitivity tests were done to ensure that the automatic *a priori* resistivities did not bias the model, and the data residuals were lowest with the automatic values. Figures 7.8 and 7.9 show an example of resistivity values for a sounding before and after inversion for the 25 layer model.

7.2.7 Residuals

The Workbench inversions output data residuals for each sounding and total residuals for the entire line. These measure how closely the model fits the data. Residuals are normalized to one standard deviation, so residuals close to 1 or below are ideal. High residuals are due to noisy data, sharp lithologic contacts, flight altitude, or very high resistivities. An example

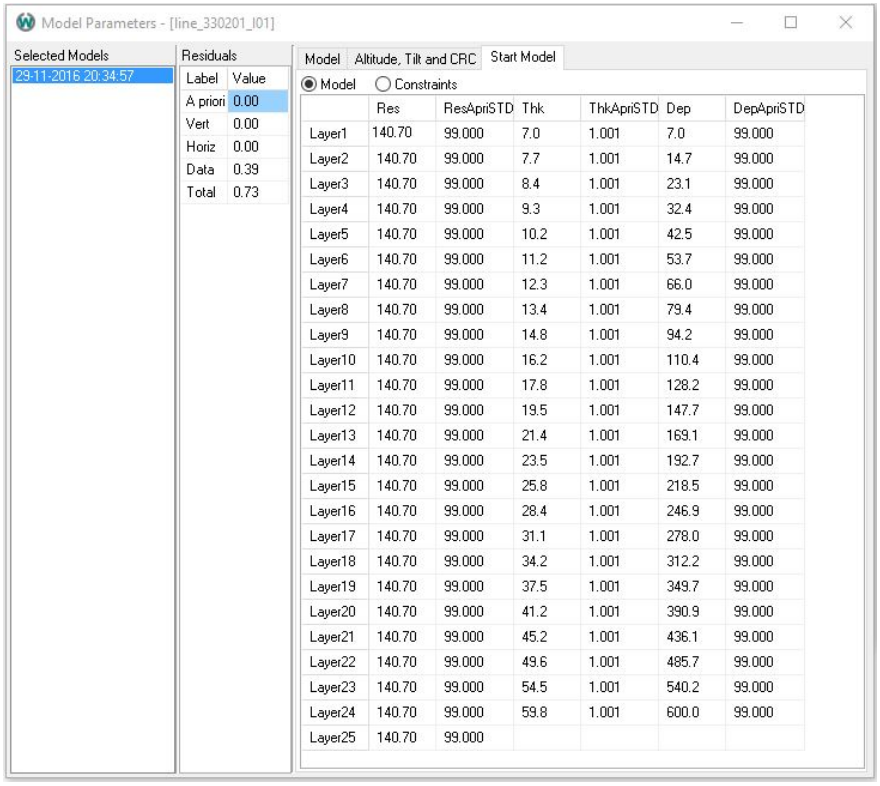

	Res	ResAprSTD	Thk	ThkAprSTD	Dep	DepAprSTD
Layer1	140.70	99.000	7.0	1.001	7.0	99.000
Layer2	140.70	99.000	7.7	1.001	14.7	99.000
Layer3	140.70	99.000	8.4	1.001	23.1	99.000
Layer4	140.70	99.000	9.3	1.001	32.4	99.000
Layer5	140.70	99.000	10.2	1.001	42.5	99.000
Layer6	140.70	99.000	11.2	1.001	53.7	99.000
Layer7	140.70	99.000	12.3	1.001	66.0	99.000
Layer8	140.70	99.000	13.4	1.001	79.4	99.000
Layer9	140.70	99.000	14.8	1.001	94.2	99.000
Layer10	140.70	99.000	16.2	1.001	110.4	99.000
Layer11	140.70	99.000	17.8	1.001	128.2	99.000
Layer12	140.70	99.000	19.5	1.001	147.7	99.000
Layer13	140.70	99.000	21.4	1.001	169.1	99.000
Layer14	140.70	99.000	23.5	1.001	192.7	99.000
Layer15	140.70	99.000	25.8	1.001	218.5	99.000
Layer16	140.70	99.000	28.4	1.001	246.9	99.000
Layer17	140.70	99.000	31.1	1.001	278.0	99.000
Layer18	140.70	99.000	34.2	1.001	312.2	99.000
Layer19	140.70	99.000	37.5	1.001	349.7	99.000
Layer20	140.70	99.000	41.2	1.001	390.9	99.000
Layer21	140.70	99.000	45.2	1.001	436.1	99.000
Layer22	140.70	99.000	49.6	1.001	485.7	99.000
Layer23	140.70	99.000	54.5	1.001	540.2	99.000
Layer24	140.70	99.000	59.8	1.001	600.0	99.000
Layer25	140.70	99.000				

Figure 7.8: Final model values seen for line 330201 in Yellowstone

of the output data and total residuals can be seen in Figure 7.9

In the Geyser Basins, the total residuals are generally higher than 1, likely due to the complex resistivity contrasts seen in the area as well as the long line lengths (up to 26 km). Total residuals in this area vary from below 1 to nearly 1.8. More expertise and processing are necessary to lower these redsiduals.

The data residuals in Norris Basin are all below 1, close to 0.6. These are more reliable models than the Geyser Basins.

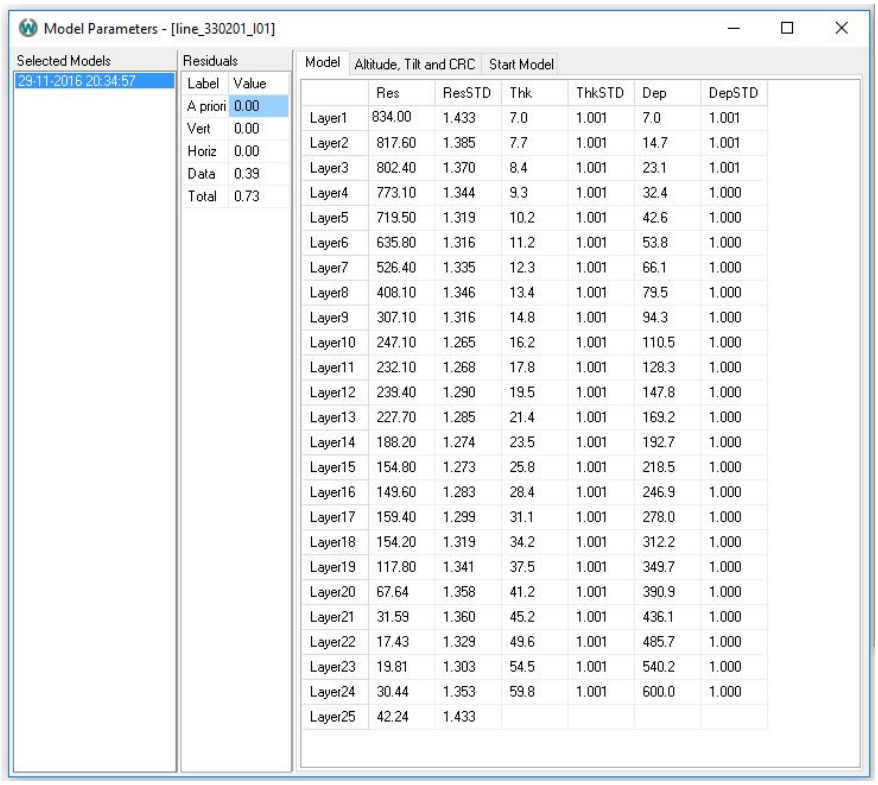

	Res	ResSTD	Thk	ThkSTD	Dep	DepSTD
Layer1	834.00	1.433	7.0	1.001	7.0	1.001
Layer2	817.60	1.385	7.7	1.001	14.7	1.001
Layer3	802.40	1.370	8.4	1.001	23.1	1.001
Layer4	773.10	1.344	9.3	1.001	32.4	1.000
Layer5	719.50	1.319	10.2	1.001	42.6	1.000
Layer6	635.80	1.316	11.2	1.001	53.8	1.000
Layer7	526.40	1.335	12.3	1.001	66.1	1.000
Layer8	408.10	1.346	13.4	1.001	79.5	1.000
Layer9	307.10	1.316	14.8	1.001	94.3	1.000
Layer10	247.10	1.265	16.2	1.001	110.5	1.000
Layer11	232.10	1.268	17.8	1.001	128.3	1.000
Layer12	239.40	1.290	19.5	1.001	147.8	1.000
Layer13	227.70	1.285	21.4	1.001	169.2	1.000
Layer14	188.20	1.274	23.5	1.001	192.7	1.000
Layer15	154.80	1.273	25.8	1.001	218.5	1.000
Layer16	149.60	1.283	28.4	1.001	246.9	1.000
Layer17	159.40	1.299	31.1	1.001	278.0	1.000
Layer18	154.20	1.319	34.2	1.001	312.2	1.000
Layer19	117.80	1.341	37.5	1.001	349.7	1.000
Layer20	67.64	1.358	41.2	1.001	390.9	1.000
Layer21	31.59	1.360	45.2	1.001	436.1	1.000
Layer22	17.43	1.329	49.6	1.001	485.7	1.000
Layer23	19.81	1.303	54.5	1.001	540.2	1.000
Layer24	30.44	1.353	59.8	1.001	600.0	1.000
Layer25	42.24	1.433				

Figure 7.9: Final model values seen for line 330201 in Yellowstone

7.2.8 Aeromagnetics

Aeromagnetic data was also acquired in the airborne survey. The magnetometer measures the total magnetic field of the area which includes the Earth's magnetic field and the regional magnetic field. It is processed down to the residual magnetic field which shows the magnetic anomalies in the area. Aeromagnetics is useful for detecting geologic boundaries, mapping source depths, and delineating faults and fractures. We use magnetics coupled with Em data to understand the physical properties driving resistivities down since both resistivity and magnetics show low anomalies over hydrothermally active areas.

General Filtering of Raw Magnetic Data

The following corrections were applied to the aeromagnetic data:

- Correction for diurnal variation using the digitally recorded ground base station magnetic values
- IGRF (International Geomagnetic Reference Field) correction
- Reduction to pole correction
- Lag was negligible therefore no lag correction was applied
- Heading was negligible therefore no heading correction was applied

Gridding

The Oasis montaj software package made by Geosoft has many gridding algorithms to choose from when interpolating magnetic data. Minimum Curvature was chosen for this dataset because it output the smoothest surface, and had nearly the same output as the bidirectional

gridding technique. The minimum curvature technique is an iterative method that fits a minimum curvature surface to the data. The plots shown in this thesis have a grid cell size of 120 m which is between $\frac{1}{3}$ and $\frac{1}{4}$ of the wider line spacing. This was the size that gridded both line spacings (450 m and 150 m) with minimal gridding artifacts. Smaller grid cell sizes were used to check if there was a large difference in the densely gridded areas (150 meter line spacing) when using smaller gird sizes, but the differences were minimal, therefore 120 meter grid cell spacing was used for the entire dataset. More information on gridding can be found in the advanced mapping how-to guide from Geosoft (2014).

Filtering

Many filtering techniques were applied to the residual magnetic field to locate general magnetic trends to correlate with the resistivity data. The most applicable to the goals of this project were upward continuation and low pass filters, which showed a correlation between magnetic and resistive lows in hydrothermal areas. Filtering the data was necessary because the residual magnetic field is very sensitive to surface geology, which is already well mapped in this area. By limiting the high frequency magnetic data, we are able to view deeper structures in the magnetic data that were covered up by surficial geology. The other filtering techniques will not be discussed in this paper.

Oasis Montaj was used for the filtering of magnetic data. The most useful filtering option was "interactive filtering" which allowed us to view the residual magnetic field and interactively add filters at different degrees. For example, when using upward continuation, rather than making one map at a time for each upward continuation depth, the interactive filter allowed us to visualize the upward continued map for upward continuations for any distance by dragging a bar. More information about Oasis Montaj MAGMAP can be found at *Applying Filters and Inverse FFT in MAGMAP*, the tutorial from Geosoft.

Low Pass Filters

Figures 3.2 and 3.1 show magnetic and resistivity data for flight lines over the Geyser Basins and Norris. The magnetic profile was calculated in Oasis Montaj using a low pass filter of 500 meters, which limited the high frequency surficial magnetic respond for both lines without over-smoothing the response. This filter was applied using the FFT option in Oasis Montaj and was applied to the database for all selected lines.

Upward Continuation

Upward continuation is a filtering technique applied to magnetic data that extrapolates magnetic measurements upward in order to see deep, dominant magnetic trends in the subsurface. For example, an upward continuation of 1000 meters mathematically shifts the observation points of the receiver up 1000 meters from terrain surface, causing the high frequency surficial trends to be ignored. Upward continuation at various heights was applied to the residual magnetic field (reduced to pole) using the MAGMAP add-on in Oasis Montaj. The results of a few of these can be seen in Figure 7.10. This figure shows the Norris RMF upward continued by 400 m, 600 m, 800 m, and 1000 m. As the upward continuation increases in distance, the more detailed, high frequency anomalies are lost.

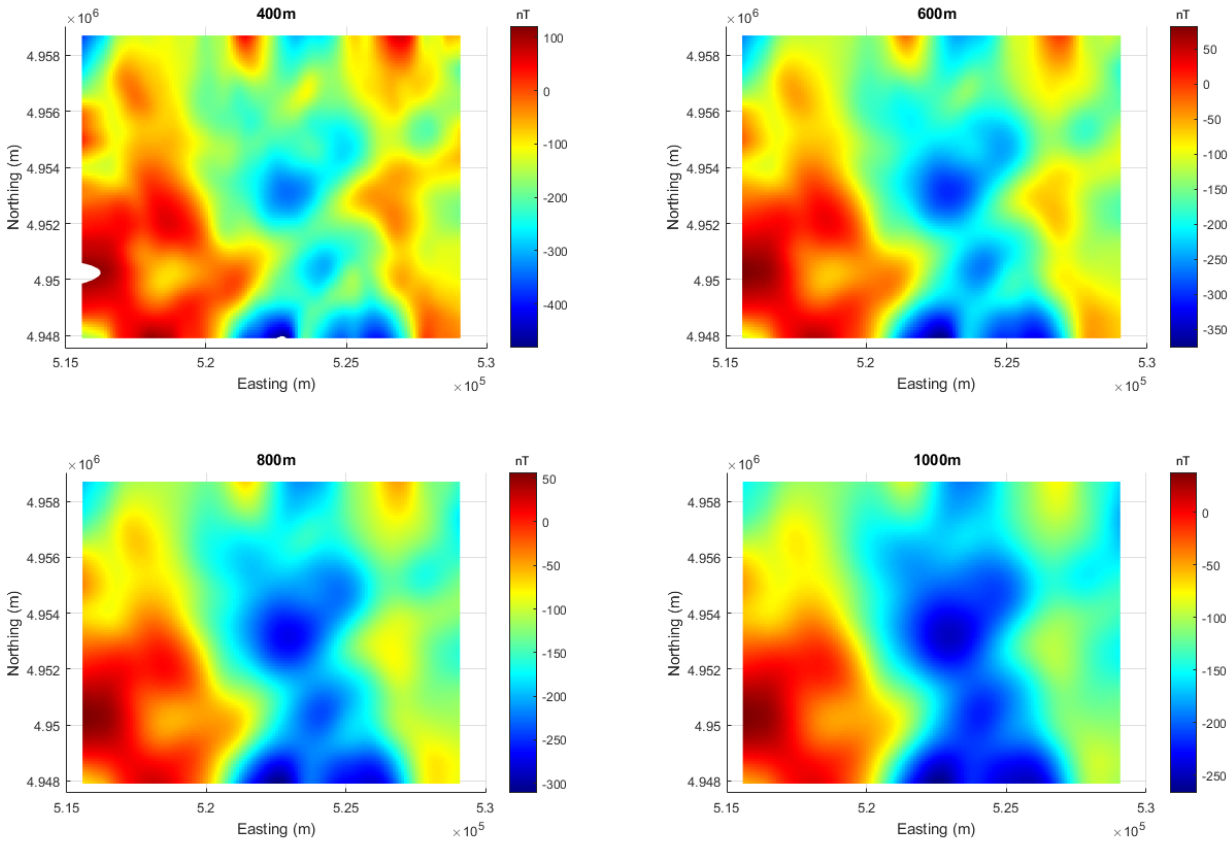

Figure 7.10: Norris RMF upward continued by 400 m, 600 m, 800 m, and 1000 m

Appendix C

8.1 MATLAB Codes

8.1.1 MATLAB Code for Rock properties calculations

The following code was used to generate figures 3.3 and 3.4. We use Archie's law for a saturated rock to calculate the resistivity with variations in temperature and porosity given specific salinities. We also plot the measured down-hole temperatures with their corresponding resistivity value at the same depths within the hole. The resistivity is taken from the nearest 1-D sounding from the airborne EM survey to each drillhole, and the temperature at each depth corresponds to a resistivity at each depth.

```
close all;
clear all;


xi = linspace(0, 80, 81);
temp_const = interp1([0 81], [70 160], xi, 'log');
ni = 12;
phi_const_a = linspace(5,60,ni);
```

```
phi_const = repmat(phi_const_a, 81,1);

% formation factor F = a*phi^(-m) from Ahmed and Revil
a = 2.4;
m = 2.12;

F = a*(phi_const./100).^(-m);



%% porosity, temp, res plot;
phi_rep = [];
phis = linspace(1,70,81);
phi_rep = repmat(phis, 81,1);

F_all = a*(phi_rep./100).^(-m);

% fluid resistivity: pw = pw0/(1+alpha(T - T0))
% alpha determined from Schlumberger salinity, res, temp plot, 250 ppm NaCl
pw_test = 20./(1+0.06*(temp_const-25));
% alpha determined from Schlumberger salinity, res, temp plot, 4000 ppm NaCl
%pw_test = 1.35./(1+0.024*(temp_const-25));
%plot(xi,temp_i);
temp_rand = linspace(50, 200, 81);
pw_test = 43./(1+0.06*(temp_rand-25));

for i = 1:81
```

```
    res_all(:,i) = F_all(:,i).*pw_test';
end;

%contours
v = [0.5 1 1.5 2 2.5 3 3.5 4];

%resistivity at temperature 50-250 deg C and porosity 0-70%
figure (1)
surfc(phis, temp_rand,log10(res_all));
hold on;
[C, h] = contour3(phis, temp_rand,log10(res_all),v, 'k');
hcb=colorbar;
title(hcb,'log_{10}Resistivity \Omegam')
colormap('jet')
caxis([0 4])
view([0 90])
%clabel(C,h)
shading flat;
xlabel('Porosity %')
ylabel('Temperature \circ C');
title('Resistivity, Porosity, and Temperature');

%% Plot actual temperatures and calculated resistivity line

%import temperature data
data = importdata('Temp_all_lines.txt');
```

```
%define porosity constant
phi_const_temp = 0.3;

%set temperature range
temps = linspace(10,250,240);

%calculate resistivity at constant porosity and variable temperature
pw = 43./(1+0.06*(temps-25));
p_phi_const = a*phi_const_temp^(-m)*pw;

%sort data input
depth = data.data(:,1);
temp = data.data(:,2);
res = data.data(:,3);

figure (2)
scatter(res,temp);
hold on;
plot(p_phi_const,temps);
set(gca,'XScale','log')
xlim([1 3000])
xlabel('Resistivity log_{10}(\Omega m)');
ylabel('Temperature (\circ C)');
title('Resistivity vs. Temperature for drillholes');
legend('Drillhole Data', 'Saturated Rock 20% Porosity',
```

```
'Saturated Rock 30% Porosity')
```

8.1.2 Resistivity Profiles

The following code (created by W. Steven Holbrook and Kira Dickey) was used to plot the 2D resistivity lines using the output .xyz file from Workbench, along with the 1-D resisivity soundings at drillhole locations and their temperatures. It also calculates average resistivity per 1-D sounding for both the interpolated data and raw data, as well as depth based conductance over the lines. Inputs for this code include the .xyz file from Workbench which has resistivities over the 2D line, the temperature file for each drillhole, and a 1D resistivity file for each drillhole which was calculated using the code in section 8.1.4.

```
% Read in .csv table with output of Workbench inversion


clear all; close all; clc;


%Table = importdata('Q_line_313501_I01_inv.xyz'); % Y-7
%Table = importdata('Q_line_336801_I01_inv.xyz'); %between Y-7 and Y-8;
Table = importdata('Q_line_336901_I01_inv.xyz'); %between Y-8;
%Table = importdata('Q_line_338401_I01_inv.xyz'); %Y-1 and C-1
%Table = importdata('Q_line_312701_I01_inv.xyz'); %near Y-5; -13.5 km
%Table = importdata('Q_line_331701_I01_inv.xyz'); % Y-2@ -1.29 km
%Table = importdata('Q_line_311601_I02_inv.xyz'); % Y-3@ 9.88 km
%Table = importdata('Q_line_311301_I01_inv.xyz'); % Y-13@
```

```
%Table = importdata('Q_line_131701_I01_inv.xyz'); % Norris near Y-9
%Table = importdata('Q_line_131401_I01_inv.xyz'); % Norris just N of
Y-12 @ 2.55 km
%Table = importdata('Q_line_131601_I01_inv.xyz'); % Norris C-2
%Table = importdata('Q_line_116601_I03_inv.xyz'); %Norris
%Table = importdata('Q_line_337101_I01_inv.xyz');

dz = 5; minDepth = 3.5; maxDepth = 300; Depth_interp = minDepth:dz:maxDepth;
% Depth_interp = 1600:5:2450;
Depth_interp=Depth_interp';

UTM_x = Table.data(:,1);
UTM_y = Table.data(:,2);
Elev = Table.data(:,3);

%Distance along line in km
Distance = sqrt((UTM_x-UTM_x(1)).^2+(UTM_y-UTM_y(1)).^2)./1000;

dx = .020; xinterp = Distance(1):dx:Distance(end); xinterp=xinterp'; %dx in km
nx = size(xinterp,1);
% Table = importdata('/Users/sholbrook/Dropbox/Norris .xyz
files/Q_line_116401_I01_inv.xyz'); % Norris N of Y-12

numLayers = Table.data(1,8);
numSoundings = length(Table.data(:,1));
```

```
UTMx_interp=interp1(Distance,UTM_x,xinterp);
UTMy_interp=interp1(Distance,UTM_y,xinterp);

%% Determine depths of each layer
    Depth_midlayer = zeros(numLayers,1);
    for jj = 1:numLayers-1
        Thickness(jj) = Table.data(1,11+(jj-1)*6);
        if(jj==1); Depth_midlayer(jj) = Thickness(jj)/2; end
        Depth_midlayer(jj+1) = Depth_midlayer(jj) + Thickness(jj);
    end
%%  Create a 3-column matrix of x,z,res
    % Res_All = zeros(numLayers,numSoundings);
    %If want a grid of scattered resistivity model
    Res_triplets = zeros(numSoundings*numLayers,3); k=1;
    for ii = 1:numSoundings
        DOI_lower(ii) = Table.data(ii,5); DOI_upper(ii) = Table.data(ii,4);
        for jj = 1:numLayers
            Res_All(jj,ii) = Table.data(ii,9+(jj-1)*6);
            Res_triplets(k,1) = Distance(ii);
            Res_triplets(k,2) = Depth_midlayer(jj);
    %         Res_triplets(k,2) = 2400-Depth_midlayer(jj);
    %         Res_triplets(k,2) = Elev(ii)-Depth_midlayer(jj);
            Res_triplets(k,3) = Table.data(ii,9+(jj-1)*6);
%             if(Res_triplets(k,2) > DOI_lower(ii)); Res_triplets(k,3)=0; end;
%Zero out values below DOI
            k=k+1;
```

```
        end
    end
    DOI_lower = DOI_lower'; DOI_upper=DOI_upper'; DOI_lower =
    interp1(Distance,DOI_lower,xinterp);DOI_upper =
    interp1(Distance,DOI_upper,xinterp);

%% Grid the data.
% I grid data in depth, not elevation - gridding doesn't work
% very well if I shift the depths to correct for surface elevation.
% Will do the shift after gridding.

    Res_GridInterp = zeros(size(Depth_interp,1),nx);
 % Res_GridInterp = griddata(Res_triplets(:,1),Res_triplets(:,2),
% Res_triplets(:,3),xinterp,Depth_interp','cubic');

    F=TriScatteredInterp(Res_triplets(:,1),Res_triplets(:,2),Res_triplets(:,3));
    [xq,yq] = meshgrid(xinterp,Depth_interp);
    Res_GridInterp = F(xq,yq);
    Res_GridInterp_300 = Res_GridInterp;

% Zero out below DOI
        for ii = 1:size(Res_GridInterp,2)
        for jj = 1:size(Res_GridInterp,1)
            if(jj*dz > DOI_lower(ii)); Res_GridInterp(jj,ii)=0; end;
            %Zero out values below DOI
        end
```

```
    end

%% Plot
figure(1); close(1); figure(1);

% colormap(autumn);
    clims=([0 3]);
    imagesc(xinterp,Depth_interp,real(log10(Res_GridInterp)),clims);
%     clims=([0 3]); imagesc(real(log10(Res_GridInterp)),clims);
    colorbar;
    xlabel(['Distance (m)','FontSize',14]);
    ylabel(['Depth (m)','FontSize',14]);
    ylabel(colorbar, 'Log Resistivity ohm-m'); hold on;


%% Shift the data to correct for elevation.

    nz = round((max(Elev) - min(Elev) + maxDepth)/dz +1);
    % Determine size of new grid using elevation
    elev_interp = interp1(Distance,Elev,xinterp);

    Res_gridShift = zeros(nz,nx);

    for i = 1:size(Res_GridInterp,2)        % loop over x
        shift_sounding(i) = round((elev_interp(i)-min(elev_interp))/dz);
        for j = 1:size(Res_GridInterp,1)   % loop over z
```

```
            Res_gridShift(size(Res_gridShift,1)-shift_sounding(i)-(j-1),i)
            = Res_GridInterp(size(Res_GridInterp,1)-j+1,i);
        end
    end
%     z_axis_shifted=round((min(Elev)+max(Depth_interp)))+
%(nz-1)*dz:-dz:round((min(Elev)+max(Depth_interp)));
    z_axis_shifted=round(max(Elev)):-dz:round(max(Elev)-(nz-1)*dz);

%% Plot

load('cmap.mat');
% cmap.mat is a color scale with 0 values set to white
figure;
subplot(1,4,[1 3])
    if (UTM_x(2)-UTM_x(1)>0)
        clims=([0 3]);
        imagesc(UTMx_interp, z_axis_shifted,real(log10(Res_gridShift)),clims);
        hold on;
        plot(Distance,-Elev,'k','LineWidth',1); %If flown west-to-east
    else
        clims=([0 3]);
        imagesc(-xinterp,-z_axis_shifted,real(log10(Res_gridShift)),clims);
        hold on;
        plot(-Distance,-Elev,'k','LineWidth',1); % If flown east-to-west
    end
```

```
    colorbar; xlabel(['Distance (km)'],'FontSize',14);
    ylabel(['Elevation (m)'],'FontSize',14);
    ylabel(colorbar, 'Resistivity (log_{10} \Omegam)','FontSize',14);
    hold on;
%  plot(xinterp,DOI_lower,'k-');
    colormap(cmap);
   %xlim([-0.4 0])
   %ylim([-2250 -1900])
    daspect([1 1000 1000]);


temp = csvread('Y12_temp.csv', 1,0);
resdata = csvread('Y12_depth_res.csv');


temps = temp(:,3);
dep = temp(:,2);
res = resdata(:,2);
depth_res = resdata(:,1);


subplot(1,4,4)
stairs(res,depth_res,'Color','r')
set(gca,'YDIR', 'reverse');
set(gca, 'XScale', 'log');
ylim([0 350])
xlim([1 1000])
xlabel('Resistivity (\Omegam)')
ylabel('Depth (m)')
```

```
ax1 = gca;
ax1.XColor = 'r';
ax1.YColor = 'k';
ax1_pos = get(ax1,'Position');
%set(ax1,'YDIR', 'reverse');
ax2 = axes('Position',ax1_pos,...
    'XAxisLocation','top',...
    'YAxisLocation','right',...
    'Color','none');
ax2.XColor = 'b';
hold on
scatter(temps,dep,'Parent',ax2)
hold on;
line(temps, dep,'Parent',ax2,'Color',  'b');
set(gca,'YDIR', 'reverse');
ylim([0 350])
xlim([0 250])
xlabel('Temperature (\circC)')
ylabel('Depth (m)')



%% Average of resistivities from raw data
% res_avg = [];
% Res_All = Res_All(1:24,:);
%
% for i=1:23
```

```
%     DEPTH(:,i) = Table.data(:,6*(i) + 7);
% end;
% zeros = zeros(253,1);
% DEPTH = [zeros, DEPTH];
% DEPTH = DEPTH(1,:);
%
% rho_vec = [];
% for i = 1:length(DEPTH)
%      one_vec = ones(round(Thickness(1,i)),1)*Res_All(i,:);
%      rho_vec = vertcat(rho_vec,one_vec);
% end;
%
% % zero DOI
%
% for ii = 1:size(Res_GridInterp,2)
%      for jj = 1:size(Res_GridInterp,1)
%             if(jj > DOI_lower(ii)); Res_GridInterp(jj,ii)=0; end;
%Zero out values below DOI
%       end
% end
%
% rho_vec(rho_vec==0) = nan;
%
% res_avg_raw = nanmean(rho_vec,1);
%
% figure (2)
```

```
% plot(UTM_x,res_avg_raw);
% %daspect([1 300 100]);
% %xlim([516000 528500])
% xlabel('Distance (km)');
% ylabel('Resistivity (\Omegam)')
% title('Average Resistivity')

%% average from interpolated data including DOI
res_avg = [];

Res_GridInterp(Res_GridInterp==0) = nan;

res_avg = nanmean(Res_GridInterp,1);

plot(UTMx_interp,res_avg);
xlim([516000 528500])
xlabel('Distance (km)');
ylabel('Resistivity (\Omegam)')
title('Average Resistivity')

%% depth integrated conductance
for i = 1:length(Thickness);
    cond_depth = sum(1/Res_All(i,1) * Thickness(i));
end;

%or..
```

```
Cond_thk = dz.*1./Res_GridInterp_300;
Cond_thk(Cond_thk == Inf) = nan;

for i = 1:length(Res_GridInterp_300)
    cond_depth(i) = nansum(Cond_thk(:,i));
end;

plot(UTMx_interp, cond_depth)
%xlim([516000 528500])
xlim([508300 516000])
set(gca, 'YScale', 'log');
xlabel('UTM12N (m)');
ylabel('Depth Integrated Conductivity(S)')
title('Conductance')


%% plot line with UTM
clims=([0 3]);
imagesc(UTMx_interp,-z_axis_shifted,real(log10(Res_gridShift)),clims);
hold on;
plot(Distance,-Elev,'k','LineWidth',1);
colorbar;
xlabel(['UTM X (m)'],'FontSize',14);
ylabel(['Elevation (m)'],'FontSize',14);
ylabel(colorbar, 'Resistivity (log_{10} \Omegam)','FontSize',14);
hold on;
```

```
colormap(cmap);
%xlim([-0.4 0])
%ylim([-2250 -1900])
daspect([1 1 1]);
```

8.1.3 MATLAB Code for Resistivities for Hydrothermal vs. Non-Hydrothermal Areas

The HNH code (below) takes a pair of X and Y UTM coordinates (manually entered), finds the nearest 1D sounding, and makes a 12x12 grid of soundings centered around the coordinates. It then plots the resistivity soundings on one plot (either in terms of the standard deviation, a probability density, or just 144 1D soundings). The most simple to visualize was the standard deviation. This was done in seven areas, four non-hydrothermal and four hydrothermal with a total of 1,008 1D resistivity soundings. The code below is specific for Hydrothermal Area 1 (H1).

```
 close all;
clear all;

data = importdata('Out_res_file.dat');

%input UTM coordinates
UTMX_real = 514980;
UTMY_real = 4933121;
```

```
% center 12x12 grid aroung coordinates
UTMX = UTMX_real - 300;
UTMY = UTMY_real - 52*8;

%Note UTMX coordinates are in 50 meter increments, UTMY's are 51.68 meter
%increments

%%

%find the X coordinate within the dataset that is closest to the input UTM X
[c index_x] = min(abs(data(:,1)-UTMX));
closest_x = data(index_x,1);

%loop through data and sort by finding all of the X and Y UTM coordinates
%corresponding to a 12X12 grid centered around the drillhole
B = [];
%sort through data for XUTM values
for i = 1:12
        idx = find(data(:,1) == closest_x + 50*i - 50);
        X1 = (data(idx,:));
        X1_save(:,:,i) = X1;
        B = [B; X1_save(:,:,i)];
end;

B(:,2) = floor(B(:,2));
```

```
[c index_y] = min(abs(B(:,2)-UTMY));

%find row of 12 closest Y UTM values
%separate based on 3 because the Y UTM coordinates are not spaced by an
%integer value (spaced by 51.63, jumps unevelnly every 3 soundings)

for i = 1:3
    closest_y_1(i) = B(index_y,2) + 52*i -52*2 ;
    closest_y_2(i) = B(index_y,2)+52*i + 52 - 1;
    closest_y_3(i) = B(index_y,2)+52*i + 52*4 - 2;
    closest_y_4(i) = B(index_y,2)+52*i + 52*7 - 3;
end;

closest_y = [];
closest_y = [closest_y_1, closest_y_2, closest_y_3, closest_y_4];
closest_y = closest_y(1:12);



C = [];
%sort the X sorted data by Y UTM values in the second column
for i = 1:12;
        idy = find(B(:,2) == closest_y(i))+ 3;
        Y1 = (B(idy,:));
        Y1_save(:,:,i) = Y1;
        C = [C; Y1_save(:,:,i)];
end;
```

```
%cordinate data
utms = [C(:,1), C(:,2)];
%manually check data for starting column without inf. values (col 46-83
%contain real values)
C = C(:,46:83);
C = 10.^C;  %get rid of log10 for resistivity values
C(C == inf) = 0;  %set infinite values to 0
C(C == 0) = nan; %set zero values to NaN so they aren't plotted at 0's
[r,c] = size(C);
depth = 0:10:(c-1)*10;%make depth increments

%save data to matrix to output and plot with more areas
mat_H1 = vertcat(depth, C_avg, std_C)';

%% Plots

%plot the drillhole coordinate with the soundings coordinates
figure (1)
scatter(utms(:,1), utms(:,2));
hold on;
scatter(UTMX_real, UTMY_real, '*');
xlabel('Easting (m)');
ylabel('Northing (m)');
title('Sounding and Drillhole Coordinates')
legend('Soundings', 'NH 2');
```

```
%xlim([5.2330*10^5 5.2395*10^5]);


%plot all soundings on one plot
figure (2);
%subplot(1,6,[1 2]);
subplot(1,2,1)
 for i = 1:length(C)
    stairs(depth, C(i,:));
    view([270 -90]);
    set(gca, 'YDIR','reverse');
    set(gca,'YScale','log')
    ylim([1, 10000]);
    xlim([0 700])
    hold on
 end;
xlabel('Depth (m)');
ylabel('Resistivity (\Omega m)');
title('NH 2 Resistivity Soundings');


% STD plots
std_C = nanstd(C);
subplot(1,2,2)
errorbar(depth,C_avg, std_C);
hold on
p2 = stairs(depth,C_avg);
xlim([0 700]);
```

```
ylim([1 10000]);
view([270 -90]);
set(gca, 'YDIR','reverse');
set(gca,'YScale','log')
title('Resistivity Standard Deviation for H1')
```

The following code was used to plot each area on one plot as seen in Figure 6.2.

```
 close all;
clear all;

mat_NH3 = csvread('mat_NH3.csv');
mat_NH2 = csvread('mat_NH2.csv');
mat_OF = csvread('mat_OF.csv');
mat_H1 = csvread('mat_H1.csv');
mat_NH4 = csvread('mat_NH4.csv');
mat_H2 = csvread('mat_H2.csv');
mat_NH5 = csvread('mat_NH5.csv');

%sort data into average resistivity and standard deviation for each area
depth = mat_NH4(:,1); %use area with maximum DOI
NH2 = mat_NH2(:,2);
NH3 = mat_NH3(:,2);
OF = mat_OF(:,2);
```

```
NH2_std = mat_NH2(:,3);

NH3_std = mat_NH3(:,3);

OF_std = mat_OF(:,3);

H1 = mat_H1(:,2);

H1_std = mat_H1(:,3);

H2 = mat_H2(:,2);

H2_std = mat_H2(:,3);

NH4 = mat_NH4(:,2);

NH4_std = mat_NH4(:,3);

NH1 = mat_NH5(:,2);

NH1_std = mat_NH5(:,3);


%make all data the same length by inputting NaN vlaues at the bottom of

%each sounding

nan_OF = ones(length(depth)-length(OF),1);

nan_OF(nan_OF == 1) = nan;

OF = vertcat(OF, nan_OF);

OF_std = vertcat(OF_std, nan_OF);


nan_NH2 = ones(length(depth)-length(NH2),1);

nan_NH2(nan_NH2 == 1) = nan;

NH2 = vertcat(NH2, nan_NH2);

NH2_std = vertcat(NH2_std, nan_NH2);


nan_H1 = ones(length(depth)-length(H1),1);

nan_H1(nan_H1 == 1) = nan;
```

```
H1 = vertcat(H1, nan_H1);
H1_std = vertcat(H1_std, nan_H1);

nan_H2 = ones(length(depth)-length(H2),1);
nan_H2(nan_H2 == 1) = nan;
H2 = vertcat(H2, nan_H2);
H2_std = vertcat(H2_std, nan_H2);

nan_NH4 = ones(length(depth)-length(NH4),1);
nan_NH4(nan_NH4 == 1) = nan;
NH4 = vertcat(NH4, nan_NH4);
NH4_std = vertcat(NH4_std, nan_NH4);

nan_NH1 = ones(length(depth)-length(NH1),1);
nan_NH1(nan_NH1 == 1) = nan;
NH1 = vertcat(NH1, nan_NH1);
NH1_std = vertcat(NH1_std, nan_NH1);

nan_NH3 = ones(length(depth)-length(NH3),1);
nan_NH3(nan_NH3 == 1) = nan;
NH3 = vertcat(NH3, nan_NH3);
NH3_std = vertcat(NH3_std, nan_NH3);

% STD plots
errorbar(depth,NH1, NH1_std,'color', 'y');
hold on
```

```
errorbar(depth,NH2, NH2_std, 'color', [0.54 0 0]);
hold on
errorbar(depth,NH3, NH3_std,'color', 'r');
hold on
errorbar(depth,NH4, NH4_std,'color', [0.950 0.50 0.050]);
hold on
errorbar(depth,H1, H1_std,'color', 'b');
hold on
errorbar(depth,H2, H2_std,'color', [0 0.75 0.75]);
hold on
errorbar(depth,OF, OF_std, 'color','c' );
hold on
xlim([0 700]);
ylim([1 10000]);
view([270 -90]);
set(gca, 'YDIR','reverse');
set(gca,'YScale','log')
xlabel('Depth (m)');
ylabel('Resistivity (\Omega m)');
title('Resistivity Standard Deviations for Hydrothermal and
Non-Hydrothermal Areas')
legend('NH1', 'NH2', 'NH3', 'NH4','LGB 1', 'LGB 2', 'Old Faithful');
```

8.1.4 MATLAB Code for Resistivity, Lithology, and Temperature plots

Code 1 was used to compare stratigraphy with resistivity and temperature. The example shown in the Appendix is drillhole Y-3. The code imports the 2D line inversion. The first two columns are UTM X and Y coordinates, the following columns are elevation, DOI upper and lower, depth increments, and resistivity data. After inputting the data, the code finds the coordinate pair that is closest to actual UTM coordinates of the drillhole. It then creates a vector using only the resistivity values at that location, pairs the resistivities with the lithology and temperature that corresponds to the same depth, and plots them together. Temperature data was taken from the tables in White et al. (1975) and are only the reliable measurements. The final output of this code is a subplot with Resistivity vs. Depth colored by lithology and a Temperature vs. Depth plot. The arrays for the resistivity and temperature at depths throughout the hole are used in the final code in this paper to generate figures such as Figures 3.5-3.14. The 1-D resistivity plot generated in this thesis is used to make the subplots in Figure 6.1.

```
close all;
clear all;

%data = importdata('Out_res_file.dat'); %use only if using the SCI inversion

data1 = importdata('Q_line_311601_I02_inv.xyz');
data_Y3 = data1.data;
```

```
 UTMX_Y3 = 512733;
 UTMY_Y3 = 4934557;

%% Y-3 center point

[c index_x] = min(abs(data_Y3(:,1)-UTMX_Y3));
closest_x = data_Y3(index_x,1);

[c index_y] = min(abs(data_Y3(:,2)-UTMY_Y3));
closest_y = data_Y3(index_y,2);

dist = sqrt((UTMX_Y3 - closest_x)^2 + (UTMY_Y3 - closest_y)^2);

idx = find(data_Y3(:,1) == closest_x);
X1 = (data_Y3(idx,:));
idy = find(X1(:,2) == closest_y);
Y3 = (X1(idy,:));

% Y3(Y3 == 1*10^30) = 0;
% Y3 = Y3(:,3:96);
%
% Y3 = 10.^Y3;
% Y3(Y3 == 1) = 0;
% Y3 = Y3(Y3~=0);

ELEV = data_Y3(:,3);
```

```
DOI_UP = data_Y3(:,4);

DOI_LOW = data_Y3(:,5);

NUM_LAYERS = data_Y3(:,8);

N = NUM_LAYERS(1);

M = 25;



%filter data to get only resistivities (every 6th term starting at term 9)

for i=1:N

    RHO(:,i) = Y3(:,6*(i-1) + 9);

end;


RHO = RHO';


%filter data to get only depths (every 6th term starting at term 7)

for i=1:N-1

    DEPTH(:,i) = Y3(:,6*(i) + 7);

end;


%format depth for correct dimensions

zs = 0;

DEPTH = [0, DEPTH];


%subplot(3,3,5);

stairs(DEPTH, RHO);

view([270 -90]);
```

```
set(gca, 'YDIR','reverse');

% depth = 440


 %% Y-3 Strat
rho_vec = [];
for i = 1:24
 one_vec = ones(round(DEPTH(i+1)-DEPTH(i)),1)*RHO(i);
 rho_vec = vertcat(rho_vec,one_vec);
end;

Y3_repeat = rho_vec(1:290);
%depth = 1:1:157;

%plot(depth,rho_vec);

strat1 = 42.2;  %glacial sediment (hydrothermally cemented sandstone,
siltstone, conglomerate)
strat2 = 72; %Nez Perce Rhyolite Flow
strat3 = 157; % Unnamed flow

Y3_1 = ones(42,1);
Y3_2 = ones(30,1)*2;
Y3_3 = ones(85,1)*3;
Y3_4 = ones(290-157,1) *4;
```

```
Y3_strat = vertcat(Y3_1, Y3_2, Y3_3, Y3_4);


Depth = 1:1:290;
Depth = Depth';

depth_res_strat = horzcat(Depth, Y3_repeat, Y3_strat);

g_seds = find(depth_res_strat(:,3) == 1);
gs1 = (depth_res_strat(g_seds,:));

np_flow = find(depth_res_strat(:,3) == 2);
np_flow1 = (depth_res_strat(np_flow,:));

flow = find(depth_res_strat(:,3) == 3);
flow1 = (depth_res_strat(flow,:));

sz = 70;

temp = csvread('Y3_temp.csv', 1,0)

subplot(1,2,1)
scatter(gs1(:,2), gs1(:,1), sz, 'b', '*');
```

```
hold on;
scatter(np_flow1(:,2), np_flow1(:,1), sz, 'c', '*');
hold on;
scatter(flow1(:,2), flow1(:,1), sz, 'r', '*');
set(gca, 'YDIR','reverse');
xlabel('Resistivity (Ohm-m)');
ylabel('Depth (m)')
title('Y-3');
legend('Glacial Sediments', 'Nez Perce Rhyolite Flow', 'Unnamed Flow');

subplot(1,2,2)
scatter(temp(:,2),temp(:,1));
line(temp(:,2), temp(:,1));
set(gca,'YDIR', 'reverse');
xlabel('Temperature \circ C')
ylabel('Depth (m)')
title('Y-3 Temperature')



%% Get resistivities at each temperature, output for other codes
Res_temp_all = [];
for i = 1:length(temp)
        id_res = floor(temp(i,1));
        Res_temp = (depth_res_strat(id_res,:));
        save(:,:,i) = Res_temp;
        Res_temp_all = [Res_temp_all; save(:,:,i)];
```

```
end;


Res_temp_all = [temp(:,1:2),Res_temp_all(:,2)];
```

8.1.5 Resistivity and Magnetic Depth Slices

The MATLAB code used to generate the plots comparing the upward continued magnetic data with the resistivity depth slice is shown below. The method used to pick the specific upward continued magnetic data height that corresponded best with a specific resistivity depth slice was computationally slow and time consuming. The residual magnetic field was upward continued at different values in increments of 100 meters from 100 meters to 1500 meters. Each upward continuation was read into MATLAB and the correlation for each resistivity depth slice was calculated. The selected upward continuation height (1200 meters) and resistivity depth slice (340 to 360 meters) had the highest correlation coefficient, $R^2 = 0.41$.

```
close all;
clear all;

%% Magnetic upward continuation of Norris
%import data from Oasis Montaj
mag_data = importdata('Norris_upcon1200.dat');

%sort mag data into UTM coordinates and magnetic data
UTMX_N_mag = mag_data(:,1);
UTMY_N_mag = mag_data(:,2);
N_upcon = mag_data(:,4);

%import resisticity depth slice (exported from SCI inversion from Workbench)
data = importdata('Mean_ResD_340m_360m.txt');
```

```
data = sortrows(data, 2);


%sort res data into UTM coordinates and EM data
UTMX = data(:,1);
UTMY = data(:,2);
Res = data(:,3);


% n value cutoffs between Norris and UGB, found using second part of code
% each depth layer has a different cell number that separates UGB and NGB
%280_300m
%n = 169188;
%240_260m
%n = 171785;
% no line at bottom 240-260
%n = 171828;
%n = 179000;
%400_420m
%n = 146079;
%420_440 m
%n = 139994;
%480_500
%n = 121296;
%380_400m
%n = 151878;
%320_340m
%n = 163358;
```

```
%300_320m
%n = 167045;
%340_360
n = 159821;
%360_380m
%n = 155547;

%separate data into UGB and NGB
UTMX_UGB = UTMX(1:n,:);
UTMY_UGB = UTMY(1:n,:);
UTMX_NGB = UTMX(n+1:end,:);
UTMY_NGB = UTMY(n+1:end,:);
Res_UGB = Res(1:n,:);
Res_NGB = Res(n+1:end,:);

%define min and max UTM values
xmin = min([UTMX_NGB;UTMX_N_mag]);
xmax = max([UTMX_NGB;UTMX_N_mag]);
ymin = min([UTMY_NGB;UTMY_N_mag]);
ymax = max([UTMY_NGB;UTMY_N_mag]);

%make a meshgrid from the min and max values for X and Y UTM coordinates
[xi, yi] = meshgrid(xmin:100:xmax, ymin+200:100:ymax);

%interpolate resistivity values over meshgrid
F_res = scatteredInterpolant(UTMX_NGB,UTMY_NGB,Res_NGB);
```

```
Res_i = F_res(xi,yi);

%interpolate magnetic data over meshgrid
F_mag = scatteredInterpolant(UTMX_N_mag,UTMY_N_mag,N_upcon);
Mag_i = F_mag(xi,yi);

%plot resistivity
figure;
surf(xi, yi, log10(Res_i));
hold on;
shading flat;
colormap(jet(256));
cmap = colormap;
colormap(cmap);
h = colorbar;
set(get(h, 'title'), 'string', 'log10(Ohm m)');
view(0,90);
axis equal;
xlim([515000 530000]);
xlabel('Easting (m)');
ylabel('Northing (m)');
caxis([0 3]);
title('Norris Resistivity 340-360 m')
hold off;

%plot magnetic data
```

```
figure (3);
surf(xi, yi, Mag_i);
hold on;
shading flat;
colormap(jet(256));
h = colorbar;
set(get(h, 'title'), 'string', 'nT');
view(0,90);
axis equal;
xlabel('Easting (m)');
ylabel('Northing (m)');
%caxis([0 5]);
xlim([515000 530000]);
title('Norris RMF Upward Continued 1200m')
hold off;

% %Linear Figure of magnetic/res comparison
% figure;
% %plot(log10(Res_i(:)),Mag_i(:),'x')
% xlabel('Resistivity (Ohm m)');
% ylabel('Residual Magnetic Field (nT)');
% title('Resistiviy 340-4360m vs. RMF 1200m')
% hold on
% Res_x = linspace(0,3000,15096);
% p = polyfit(log10(Res_i(:)), Mag_i(:), 1);
% s = regstats(Mag_i(:),log10(Res_i(:)),'linear');
```

```
% scatter = plot(Res_i(:),Mag_i(:),'x');
% hold on;
% line = plot(Res_x(:), p(1)*Res_x(:)+p(2));
% line.LineWidth = 5;
% xlim([0, 800]);
% ylim([-300,100]);

%Log figure
plot(log10(Res_i(:)),Mag_i(:),'x')
xlabel('log10(Resistivity) (Ohm m)');
ylabel('Residual Magnetic Field (nT)');
title('Resistiviy 340-360m vs. RMF Upward Continued 1200m')
hold on
Res_x = linspace(0,3000,15096);
p = polyfit(log10(Res_i(:)), Mag_i(:), 1);
s = regstats(Mag_i(:),log10(Res_i(:)),'linear');
hold on;
line = plot(log10(Res_x(:)), p(1)*log10(Res_x(:))+p(2),'-k');
line.LineWidth = 5;
xlim([0.5, 3]);
ylim([-500,200]);

%% PART 2: used to find NGB and UGB cutoff "n"
% use the figure to narrow down the cutoff between UGB and NGB
%return
%2D interpolated grid
```

```
% figure (1);
% [xi, yi] = meshgrid( min(UTMX_UGB):200:max(UTMX_UGB),
%min(UTMY_UGB):200:max(UTMY_UGB));
% zi = griddata(UTMX_UGB, UTMY_UGB, log(Res_UGB), xi, yi);
% surf(xi, yi, zi);
% shading flat;
% colormap(jet(256));
% h = colorbar;
% set(get(h, 'title'), 'string', 'Ohm m');
% view(0,90);
% xlabel('Easting (m)');
% ylabel('Northing (m)');
% caxis([0 5]);
% title('Geyser Basins 240-260 m')

% figure (2);
% [xiN, yiN] = meshgrid( min(UTMX_NGB):100:max(UTMX_NGB),
%min(UTMY_NGB):100:max(UTMY_NGB));
% ziN = griddata(UTMX_NGB, UTMY_NGB, log(Res_NGB), xiN, yiN);
% surf(xiN, yiN, ziN);
% shading flat;
% colormap(jet(256));
% h = colorbar;
% set(get(h, 'title'), 'string', 'Ohm m');
% view(0,90);
% xlabel('Easting (m)');
```

```
% ylabel('Northing (m)');
% title('Norris 280-300 m')
% caxis([0 5]);
```

Finding the "n" value

The value "n" is the cell number that separates the Upper Geyser Basin resistivity data form the Norris Basin data. This value is unique to each depth slice and must be calculated if you only want to use one data from one basin. Figure 8.1 shows the plot resulting from a value of "n" that is too low, separating the resistivity data within the Geyser Basins instead of between the Geyser Basins and Norris. Figure 8.2 shows the plot resulting from the correct "n" value, which comes from trial and error.

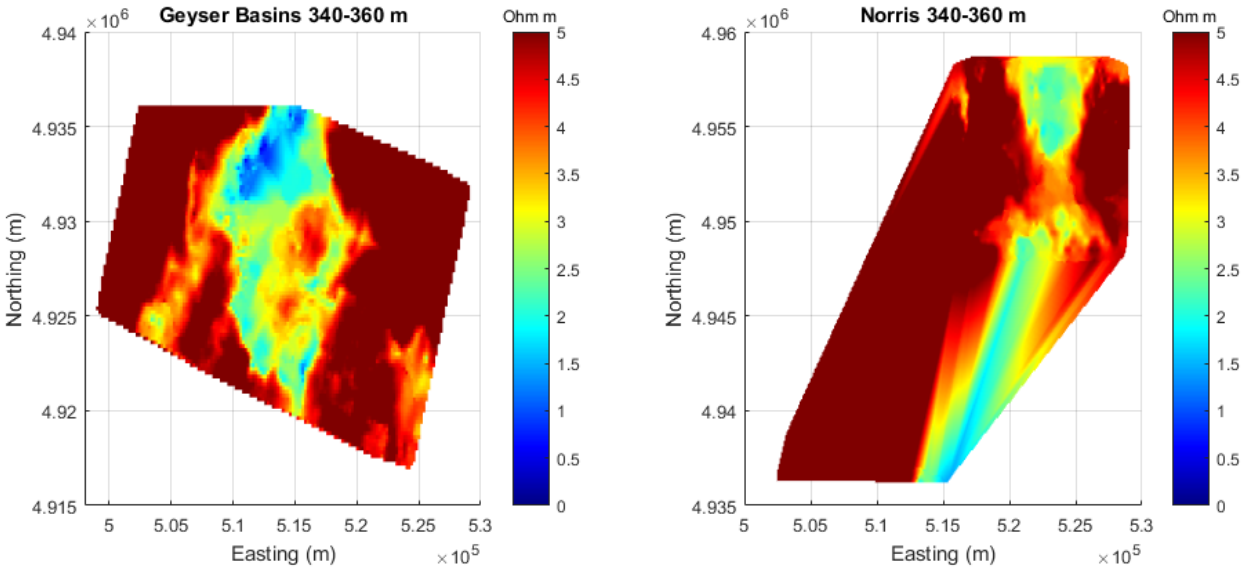

Figure 8.1: Plots used to calculate "n" value that separates Geyser Basin resistivity data from Norris Basin data

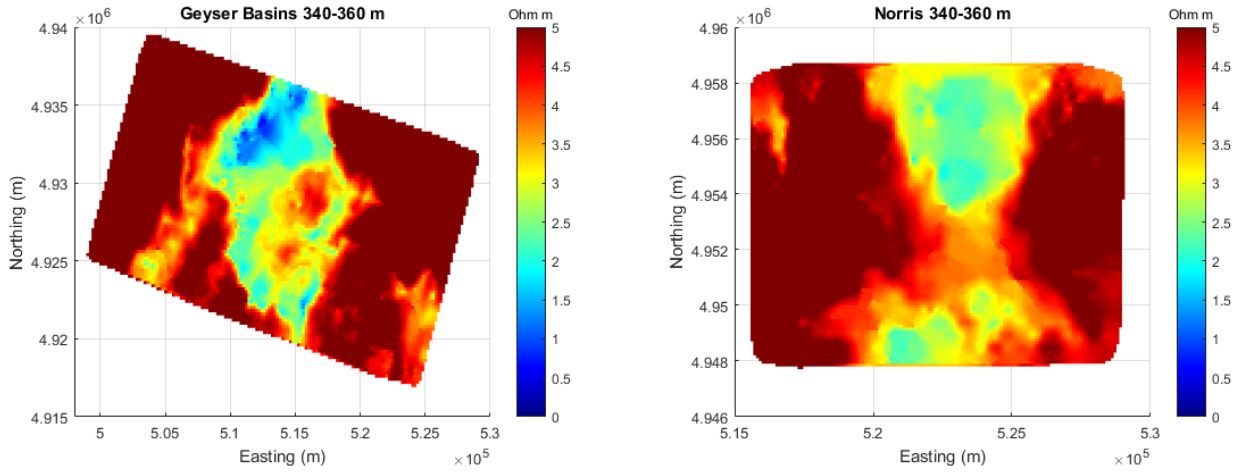

Figure 8.2: Correct "n" value plot that separates Geyser Basin resistivity data from Norris Basin data

References

Ahmed, A. S., Revil, A., Byrdina, S., Coperey, A., Gailler, L., Grobbe, N., ... others (2018). 3D electrical conductivity tomography of volcanoes. *Journal of Volcanology and Geothermal Research*, *356*, 243–263.

Archie, G. E., et al. (1942). The electrical resistivity log as an aid in determining some reservoir characteristics. *Transactions of the AIME*, *146*(01), 54–62.

Auken, E., Christiansen, A. V., Kirkegaard, C., Fiandaca, G., Schamper, C., Behroozmand, A. A., ... others (2014). An overview of a highly versatile forward and stable inverse algorithm for airborne, ground-based and borehole electromagnetic and electric data. *Exploration Geophysics*, *46*(3), 223–235.

Bargar, K. E., & Beeson, M. H. (1981). Hydrothermal alteration in research drill hole Y-2, Lower Geyser Basin, Yellowstone National Park, Wyoming. *American Mineralogist*, *66*, 473–490.

Bargar, K. E., & Beeson, M. H. (1985). *Hydrothermal alteration in research drill hole Y-3, Lower Geyser Basin, Yellowstone National Park, Wyoming* (Tech. Rep.). USGPO; For sale by the Distribution Branch, Text Products Section, US Geological Survey,.

Bibby, H., Dawson, G., Rayner, H., Bennie, S., & Bromley, C. (1992). Electrical resistivity and magnetic investigations of the geothermal systems in the Rotorua area, New Zealand. *Geothermics*, *21*(1-2), 43–64.

Björnsson, S., Arnórsson, S., & Tómasson, J. (1970). Exploration of the Reykianes thermal brine area. *Geothermics*, *2*, 1640–1650.

Bouligand, C., Glen, J. M., & Blakely, R. J. (2014). Distribution of buried hydrothermal alteration deduced from high-resolution magnetic surveys in Yellowstone National Park. *Journal of Geophysical Research: Solid Earth*, *119*(4), 2595–2630.

Browne, P. (1978). Hydrothermal alteration in active geothermal fields. *Annual review of earth and planetary sciences*, *6*(1), 229–248.

Caldwell, G., Pearson, C., & Zayadi, H. (1986). Resistivity of rocks in geothermal systems: a laboratory study. In *proceedings 8th nz geothermal workshop* (pp. 227–231).

Christiansen, A., & Auken, E. (2012). A global measure for depth of investigation. *Geophysics*, *77*(4), WB171–WB177.

Christiansen, R. L. (1984). Yellowstone magmatic evolution: Its bearing on understanding large-volume explosive volcanism. *Explosive Volcanism: Inception, Evolution, and Hazards*.

Christiansen, R. L. (2001). *The Quaternary and Pliocene Yellowstone Plateau volcanic field of Wyoming, Idaho, and Montana* (Report No. 729G). Retrieved from `http://pubs.er.usgs.gov/publication/pp729G`

Christiansen, R. L., & Blank Jr, H. R. (1972). *Volcanic stratigraphy of the Quaternary rhyolite plateau in Yellowstone National Park* (Tech. Rep.). US Geological Survey.

Dobson, P. F., Kneafsey, T. J., Hulen, J., & Simmons, A. (2003). Porosity, permeability, and fluid flow in the Yellowstone geothermal system, Wyoming. *Journal of Volcanology and Geothermal Research*, *123*(3-4), 313–324.

Fenner, C. N. (1936). Bore-hole investigations in yellowstone park. *The Journal of Geology*, *44*(2, Part 2), 225–315.

Finn, C. A., Deszcz-Pan, M., Anderson, E. D., & John, D. A. (2007). Three-dimensional geophysical mapping of rock alteration and water content at mount adams, washington: Implications for lahar hazards. *Journal of Geophysical Research: Solid Earth*, *112*(B10).

Finn, C. A., Deszcz-Pan, M., Ball, J. L., Bloss, B. J., & Minsley, B. J. (2018). Three-dimensional geophysical mapping of shallow water saturated altered rocks at mount baker, washington: Implications for slope stability. *Journal of Volcanology and Geothermal Research*, *357*, 261–275.

Finn, C. A., & Morgan, L. A. (2002). High-resolution aeromagnetic mapping of volcanic terrain, Yellowstone National Park. *Journal of Volcanology and Geothermal Research*, *115*(1-2), 207–231.

Flóvenz, Ó., Spangenberg, E., Kulenkampff, J., Árnason, K., Karlsdóttir, R., & Huenges, E. (2005). The role of electrical interface conduction in geothermal exploration. In *Proceedings of the 2005 world geothermal congress* (pp. 24–29).

Fournier, R. O. (1989). Geochemistry and dynamics of the Yellowstone National Park hydrothermal system. *Annual Review of Earth and Planetary Sciences*, *17*(1), 13–53.

Geosoft. (2014). *Oasis montaj Advanced Mapping.*

Hatherton, T., Macdonald, W. J. P., & Thompson, G. E. K. (1966). Geophysical methods in geothermal prospecting in New Zealand. *Bulletin volcanologique*, *29*(1), 485–497.

Hersir, G. P., et al. (2013). Resistivity of rocks.

Hochstein, M., & Hunt, T. (1970). Seismic, gravity and magnetic studies, Broadlands geothermal field, New Zealand. *Geothermics*, *2*, 333–346.

Honda, S. (1970). Hydrothermal alteration in core from research drill hole Y-1, Upper Geyser Basin, Yellowstone National Park, Wyoming. *American Mineralogist*, *55*, 1714-1737.

Hurwitz, S., & Lowenstern, J. B. (2014). Dynamics of the Yellowstone hydrothermal system. *Reviews of Geophysics*, *52*(3), 375–411.

Ildefonse, B., & Pezard, P. (2001). Electrical properties of slow-spreading ridge gabbros from ODP Site 735, Southwest Indian Ridge. *Tectonophysics*, *330*(1-2), 69–92.

Jarrard, R. D., & Schaar, R. (1991). Electrical properties of basalts from Sites 768 and 770. In *Proc. ocean drill. program sci. results* (Vol. 124, pp. 91–104).

Jørgensen, F., Sandersen, P. B., & Auken, E. (2003). Imaging buried Quaternary valleys using the transient electromagnetic method. *Journal of Applied Geophysics*, *53*(4), 199–213.

Keith, T. E. C., & Muffler, L. (1978). Minerals produced during cooling and hydrothermal alteration of ash flow tuff from Yellowstone drill hole Y-5. *Journal of Volcanology and Geothermal Research*, *3*(3-4), 373–402.

Keith, T. E. C., White, D. E., & Beeson, M. H. (1978). *Hydrothermal alteration and self-sealing in Y-7 and Y-8 drill holes in northern part of Upper Geyser Basin, Yellowstone National Park, Wyoming* (Report No. 1054A). Retrieved from `http://pubs.er.usgs.gov/publication/pp1054A`

Llera, F. J., Sato, M., Nakatsuka, K., & Yokoyama, H. (1990). Temperature dependence of the electrical resistivity of water-saturated rocks. *GEOPHYSICS*, *55*(5), 576-585. Retrieved from `https://doi.org/10.1190/1.1442869` doi: 10.1190/1.1442869

Munoz, G. (2014). Exploring for geothermal resources with electromagnetic methods. *Surveys in geophysics*, *35*(1), 101–122.

Nabighian, M. N., & Macnae, J. C. (1991). Time domain electromagnetic prospecting methods. *Electromagnetic methods in applied geophysics*, *2*(part A), 427–509.

Nono, F., Gibert, B., Parat, F., Loggia, D., Cichy, S. B., & Violay, M. (2018). Electrical conductivity of icelandic deep geothermal reservoirs up to supercritical conditions: Insight from laboratory experiments. *Journal of Volcanology and Geothermal Research*.

Nordstrom, D. K., McCleskey, R. B., & Ball, J. W. (2009). Sulfur geochemistry of hydrothermal waters in Yellowstone National Park: IV Acid–sulfate waters. *Applied Geochemistry*, *24*(2), 191–207.

Pasquet, S., Holbrook, S., Carr, B., & Sims, K. (2016, 11). Geophysical imaging of shallow degassing in a Yellowstone hydrothermal system.

Pezard, P. A. (1990). Electrical properties of mid-ocean ridge basalt and implications for the structure of the upper oceanic crust in Hole 504B. *Journal of Geophysical Research: Solid Earth*, *95*(B6), 9237–9264.

Pitt, A., & Hutchinson, R. (1982). Hydrothermal changes related to earthquake activity at mud volcano, Yellowstone National Park, Wyoming. *Journal of Geophysical Research: Solid Earth*, *87*(B4), 2762–2766.

Revil, A. (2012). Spectral induced polarization of shaly sands: Influence of the electrical double layer. *Water Resources Research*, *48*(2).

Revil, A., Cathles, L., Losh, S., & Nunn, J. (1998). Electrical conductivity in shaly sands with geophysical applications. *Journal of Geophysical Research: Solid Earth*, *103*(B10), 23925–23936.

Revil, A., Coperey, A., Shao, Z., Florsch, N., Fabricius, I. L., Deng, Y., ... others (2017). Complex conductivity of soils. *Water Resources Research*, *53*(8), 7121–7147.

Revil, A., Hermitte, D., Spangenberg, E., & Cochémé, J. (2002). Electrical properties of zeolitized volcaniclastic materials. *Journal of Geophysical Research: Solid Earth*, *107*(B8).

Revil, A., & Pezard, P. (1998). Streaming electrical potential anomaly along faults in geothermal areas. *Geophysical Research Letters*, *25*(16), 3197–3200.

Risk, G., Bibby, H., & Caldwell, T. (1999). Resistivity structure of the central Taupo Volcanic Zone, New Zealand. *Journal of volcanology and geothermal research*, *90*(3-4), 163–181.

Schlumberger. (2009). *Schlumberger log interpretation charts*.

Smith, R. B., & Braile, L. W. (1994). The Yellowstone hotspot. *Journal of Volcanology and Geothermal Research*, *61*(3-4), 121–187.

Smith, R. B., & Christiansen, R. L. (1980). Yellowstone Park as a window on the earth's interior. *Scientific American*, *242*(2), 104–117.

Sørensen, K. I., & Auken, E. (2004). Skytem–a new high-resolution helicopter transient electromagnetic system. *Exploration Geophysics*, *35*(3), 194–202.

Studt, F. (1959). Magnetic survey of the Wairakei hydrothermal field. *New Zealand Journal of Geology and Geophysics*, *2*(4), 746–754.

Ussher, G., Harvey, C., Johnstone, R., & Anderson, E. (2000). Understanding the resistivities observed in geothermal systems. In *proceedings world geothermal congress* (pp. 1915–1920).

Waite, G. P., & Smith, R. B. (2002). Seismic evidence for fluid migration accompanying subsidence of the Yellowstone caldera. *Journal of Geophysical Research: Solid Earth*, *107*(B9).

Waxman, M. H., Smits, L., et al. (1968). Electrical conductivities in oil-bearing shaly sands. *Society of Petroleum Engineers Journal*, *8*(02), 107–122.

White, D. E., Fournier, R. O., Muffler, L. J. P., & Truesdell, A. H. (1975). *Physical results of research drilling in thermal areas of Yellowstone National Park, Wyoming* (Report No. 892). Retrieved from `http://pubs.er.usgs.gov/publication/pp892`

White, D. E., Keith, T. E., & Hutchinson, R. A. (1988). The geology and remarkable thermal activity of Norris Geyser Basin, Yellowstone National Park, Wyoming.

Zohdy, A. A., Anderson, L., & Muffler, L. (1973). Resistivity, self-potential, and induced-polarization surveys of a vapor-dominated geothermal system. *Geophysics*, *38*(6), 1130–1144.